Tectonics

RESEARCH ARTICLE
10.1029/2021TC006841

Assembly and Tectonic Evolution of Continental Lower Crust: Monazite Petrochronology of the Ivrea-Verbano Zone (Val Strona di Omegna)

Damaris C. Wyatt[1], Andrew J. Smye[1], Joshua M. Garber[1], and Bradley R. Hacker[2]

[1]Department of Geosciences, Penn State University, University Park, PA, USA, [2]Department of Earth Science, University of California, Santa Barbara, Santa Barbara, CA, USA

Key Points:

- Metamorphic monazite growth in the Ivrea-Verbano Zone started by 316 ± 2 Ma
- Monazite in metasediments preserves a record of high-temperature decompression
- Assembly and heating of Variscan lower crust to amphibolite-to-granulite-facies conditions took <30 Myr

Supporting Information:

Supporting Information may be found in the online version of this article.

Correspondence to:

A. J. Smye,
smye@psu.edu

Citation:

Wyatt, D. C., Smye, A. J., Garber, J. M., & Hacker, B. R. (2022). Assembly and tectonic evolution of continental lower crust: Monazite petrochronology of the Ivrea-Verbano Zone (Val Strona di Omegna). *Tectonics*, *41*, e2021TC006841. https://doi.org/10.1029/2021TC006841

Received 30 MAR 2021
Accepted 25 FEB 2022

Abstract Metasediments are common constituents of exhumed lower-to-mid-crustal granulite terranes; understanding their emplacement is significant for the assembly and tectonic evolution of deep continental crust. Here, we report a monazite U-Th-Pb petrochronological investigation of the Variscan Ivrea-Verbano Zone (IVZ) (Val Strona di Omegna section)—an archetypal section of lower crust. Monazite Th-Pb dates from 11 metapelitic samples decrease with structural depth from 310 to 285 Ma for amphibolite-facies samples to <290 Ma for granulite-facies samples. These dates exhibit a time-resolved variation in monazite trace-element composition, dominated by the effects of plagioclase and garnet partitioning. Monazite growth under prograde to peak metamorphic conditions began as early as 316 ± 2 Ma. Amphibolite-facies monazite defines a trend consistent with progressively decreasing garnet modal abundances during decompression and cooling starting at ~310 Ma; the timing of the onset of exhumation decreases to ~290 Ma at the base of the amphibolite-facies portion of the section. Structurally lower, granulite-facies monazite equilibrated under garnet-present pressure-temperature conditions at <290 Ma, with monazite (re)crystallization persisting until at least ~260 Ma. Combined with existing detrital zircon U-Pb dates, the monazite data define a <30 Myr duration between deposition of clastic sediments and their burial and heating, potentially to peak amphibolite-to-granulite-facies conditions. Similarly brief timescales for deposition, burial and prograde metamorphism of lower crustal sediments have been reported from continental magmatic arc terranes—supporting the interpretation that the IVZ represents sediments accreted to the base of a Variscan arc magmatic system >5 Myr prior to the onset of regional extension and mafic magmatism.

Plain Language Summary Metamorphosed sediments are persistently present in tracts of high-temperature rock that once formed the continental lower crust. The tectonic processes responsible for entrainment and metamorphism of these rocks in the lower crust are uncertain and yet significant for understanding how the continents are stabilized. We present a detailed investigation of the metamorphic evolution of an archetypal section of former continental lower crust- the Ivrea-Verbano Zone in NW Italy. Using the age and composition of monazite growth determined for 11 metasedimentary samples along a transect, we found that these former sediments were deposited, buried to more than ~20 km depth and heated to conditions hot enough to melt in under 30 million years. Similarly short timescales for this sequence of events have been reported from metamorphosed sediments exhumed from beneath continental volcanic arcs, implying that continental arcs are important for the formation of metasedimentary lower crust.

1. Introduction

Earth's continental crust is andesitic to dacitic on average (57–66 wt% SiO_2; e.g., Hacker et al., 2015; Rudnick & Gao, 2014; Rudnick et al., 2003; Taylor & McLennan, 1985). Though the composition and physical properties of upper continental crust are well known (Rudnick & Gao, 2014; Rudnick et al., 2003, and references therein), the compositions—and formative tectonic processes—of continental middle and lower crust remain enigmatic as they can only be estimated from exhumed metamorphic terrains, xenoliths and geophysical data. The prevailing paradigm is that lower crust is predominantly mafic, based on the compositions of xenoliths entrained from lower crust and of granulite-facies terrains, inferred heat flow from lower crust, and lower crustal seismic wavespeeds (e.g., Condie, 1999; Downes, 1993; Kay & Mahlburg-Kay, 1991; Rudnick et al., 2003; Rudnick & Gao, 2014; Sammon et al., 2020). However, each of these constraints is associated with appreciable ambiguity: for example, (a) non-mafic xenoliths are preferentially assimilated during the eruption of mafic magmas, biasing the xenolith

record toward mafic compositions (e.g., Halliday et al., 1993), (b) the inferred heat flow from lower crust depends on the assumed compositions and thicknesses of other crustal layers, and on mantle heat flow—each of which are sufficiently unknown that existing heat flow constraints permit between 0% and 80% mafic rocks in the lower crust (Hacker et al., 2011), and (c) seismic wavespeeds are only diagnostic of SiO_2 content or rock type under special circumstances (Behn & Kelemen, 2003; Rudnick & Fountain, 1995), and may only require ~20% of lower crust to be mafic (Hacker et al., 2015).

In contrast to the xenolith and geophysical data, the ubiquitous presence of metasedimentary rocks in worldwide granulite terranes (e.g., Hand et al., 1994; Hart et al., 1990; Heaman et al., 2011; Hermann et al., 1997; Schenk, 1990; Truscott & Shaw, 1990) provides support for a more felsic lower crust, but also raises the question: *how are sediments incorporated into the continental lower crust?* Several mechanisms have been proposed for their emplacement: (a) burial of sediments by the combined action of sedimentation and volcanism on top (e.g., Brown & Walker, 1993); (b) underplating of sediments by contractional juxtaposition of crustal sections, with the lower plate becoming lower crust (e.g., Jacobson, 1997), and (c) relamination of buoyant slab-top sediments during subduction (Hacker et al., 2011). Discriminating among these hypotheses requires knowledge of the prograde pressure-temperature-time (*PTt*) path and peak metamorphic conditions of lower crustal metasediments—a task that is made challenging by the extreme temperatures attained in granulite terranes and the pervasively overprinted nature of exhumed rocks.

The purpose of this investigation is to derive *PTt* constraints on the prograde-to-peak metamorphic evolution of an archetypal lower-crustal metasedimentary section—the Hercynian-aged Ivrea-Verbano Zone (IVZ), northwest Italy. We report and systematically analyze a large monazite U/Th-Pb and trace-element data set collected along a structural section that spans the structural thickness of the IVZ. These data provide key constraints on (a) the duration over which pre-Permian clastic metasediments were deposited, buried, heated and assembled into the continental lower crust, and (b) the timing of the onset and duration of decompression following regional amphibolite-to-granulite metamorphism. We show that the timescales and heating rates associated with assembly of the IVZ are similar to those derived from sediments underplated beneath continental magmatic arc systems, suggesting that the incorporation of sediments into IVZ lower continental crust occurred during a late-stage, subduction-to-collision system.

2. The Ivrea-Verbano Zone

The IVZ (NW Italy) is an archetypal section of Hercynian middle-to-lower continental crust (Figure 1; Boriani & Villa, 1997; Burke & Fountain, 1990; Handy et al., 1999; Quick et al., 1995; Zingg et al., 1990). It extends ~120 km along strike and is up to 14 km wide; tilted and faulted into its current position during the Alpine collision; the IVZ is bounded to the northwest by the Insubric Line and to the southeast by the Cosseto-Mergozzo-Brissago Line (CMB; Brodie et al., 1992; Fountain, 1976; Mehnert, 1975). The Insubric Line is a 1 km-thick Oligo-Miocene mylonite belt separating the Southern Alpine block, including the IVZ, from retrogressed greenschist-facies rocks that underwent Alpine high-pressure metamorphism (e.g., Babist et al., 2006). The Permian-aged CMB line is a <6 km-wide transpressional shear zone that divides the lower-to mid-crustal IVZ from the mid-to upper-crustal Serie dei Laghi section (Boriani et al., 1990; Schmid et al., 1987). Different interpretations exist for the relationship between the IVZ and the Serie dei Laghi; some regard the two sections as a coherent cross section through continental crust (Handy et al., 1999; Henk et al., 1997; Quick et al., 2003; Zingg et al., 1990), but Boriani et al. (2016) suggested that the two crustal sections are not related, and that the Serie dei Laghi was transported into its current position by translational motion along the CMB in the early Permian.

2.1. Lithologies of the Ivrea-Verbano Zone

The IVZ comprises three dominant rock units: (a) supracrustal rocks of the Kinzigite Formation, (b) ultramafic rocks, and (c) broadly gabbroic rocks of the Mafic Complex (Figure 1). The Kinzigite Formation is the focus of this investigation and is dominated by siliciclastic metasediments of pelitic-to-psammitic composition (Redler et al., 2012) with minor quartzite, calcsilicate and carbonate components (Figure 1). Metamorphic grade within the Kinzigite Formation spans amphibolite-facies in the southeast to granulite-facies in the northwest, defining a metamorphic field gradient perpendicular to the dominant planar fabric (Schmid & Wood, 1976). Previous workers have subdivided the Kinzigite Formation into amphibolite- and granulite-facies domains; amphibolite-facies

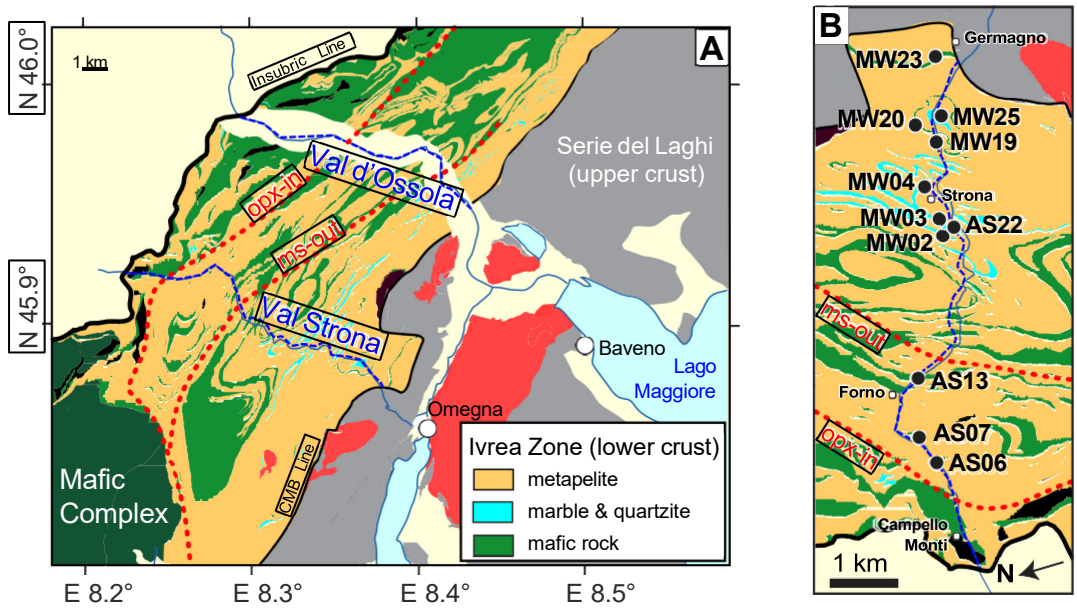

Figure 1. Geological map of the Ivrea-Verbano zone (panel A) around Val Strona di Omegna and Val d'Ossola. Modified from Brack et al. (2010); the muscovite→K-feldspar isograd in sillimanite-bearing paragneisses and the orthopyroxene-in isograd in mafic rocks are from Zingg (1980). Panel B shows sample localities along Val Strona di Omegna in order of increasing (from top-to-bottom) metamorphic grade.

metasediments are colloquially termed "kinzigites," whereas granulite-facies metasediments are termed "stronalites" (Schnetger, 1994). Following Redler et al. (2012), we emphasize that both these terms are exclusively applied to the metasedimentary rocks despite their intercalation with other rock types. All rocks are intruded by the voluminous Mafic Complex—a regional gabbroic to dioritic intrusion (100 km along strike and up to 10 km wide) that was emplaced within the IVZ section some ~30 Myr after the thermal climax of regional high-temperature metamorphism (Barboza & Bergantz, 2000; Barboza et al., 1999; Karakas et al., 2019; Klötzli et al., 2014; Quick et al., 2003). Despite rift-related deformation and heating during the Triassic and Jurassic (Handy et al., 1999) as well as Alpine collision, retrogressive overprinting is restricted to macroscale shear zones (Schmid, 1993) and resetting of rutile U-Pb dates (Ewing et al., 2015; Smye et al., 2019).

The Kinzigite Formation is stratigraphically thick and well exposed along Val Strona di Omegna (Figure 1), which is the geographic target of this investigation. Kinzigites and stronalites are predominately aluminous metapelites (53–60 wt. % SiO_2), with subsidiary metapsammites (50–77 wt. % SiO_2) and metagreywackes (e.g., Redler et al., 2012). From amphibolite-to granulite-facies conditions, the metamorphic field gradient within the IVZ metapelites is defined by decreasing abundance of muscovite and increasing abundance of alkali feldspar and garnet in metapelites; the onset of granulite-facies conditions is marked by a sharp decrease (/increase) in biotite(/garnet) mode according to the generalized reaction: biotite + plagioclase + sillimanite + quartz = garnet + K-feldspar + rutile + water/melt. Sillimanite is common throughout the IVZ either as fibrous mats associated with biotite in the amphibolite-facies portion of the section, or as prismatic mm-to cm-sized crystals in the granulites (Schmid & Wood, 1976). Stronalite bulk compositions are restitic and consistent with between 20 and 40 wt.% loss of a granitic melt component from kinzigite precursors (Schnetger, 1994).

In metabasic rocks of the Kinzigite Formation, increasing metamorphic grade in hornblende and plagioclase bearing rocks results in the appearance of clinopyroxene + orthopyroxene at the expense of hornblende + plagioclase at progressively deeper structural levels (Kunz & White, 2019; Zingg, 1980). Prismatic hornblende changes from green to brown from amphibolite to granulite facies (Sills & Tarney, 1984). The changes in the mineralogy of metabasic rocks are partly due to the metamorphic field gradient as well as changes in protolith composition across the strike of the IVZ: metabasites near the Insubric Line are depleted in light rare earth elements (LREE), consistent with a depleted N-MORB protolith, whereas metabasites at higher structural levels have enriched LREE patterns compatible with an enhanced-MORB protolith (Mazzucchelli & Siena, 1986). The metabasites also transition texturally from nematoblastic to granoblastic with increasing grade (Zingg, 1980).

Ultramafic rocks are also present as hectometer-to-decameter scale lenses in the lowermost structural levels of the Kinzigite Formation; they are dominated by spinel lherzolite and minor pyroxenite with several generations of crosscutting pyroxenite dikes (Boriani & Giobbi, 2004; Quick et al., 2003; Sills & Tarney, 1984). These ultramafic bodies are conventionally interpreted as tectonic slices incorporated into an accretionary prism prior to the intrusion of the Mafic Complex (Quick et al., 1995) or differentiates formed in the upper mantle (Rivalenti, 1975).

Initial efforts to quantify metamorphic conditions focused on the application of garnet-biotite Fe–Mg exchange thermobarometry to metapelites (Henk et al., 1997; Schmid & Wood, 1976), but recently applied single-phase solution thermometers (Zr-in-rutile, Ti-in-zircon) show that stronalites preserve peak metamorphic temperatures between 850 and 1,000°C (Ewing et al., 2013; Luvizotto & Zack, 2009). Phase equilibria modeling constrains peak *PT* conditions to ~3.5–6.5 kbar and 650°C–730°C in kinzigites from the top of the section to ~10–12 kbar and 900°C–950°C in stronalites from the deepest structural levels (Redler et al., 2012), which is further supported by thermobarometry on amphibolites intercalated throughout the section (Kunz & White, 2019). These data corroborate previous work showing that the metamorphic field gradient is significantly attenuated relative to undisturbed continental crust (~0.3 kbar/km; Burke & Fountain, 1990), implying that the section was thinned following high-temperature metamorphism (Brodie et al., 1989; Brodie & Rutter, 1987; Henk et al., 1997).

2.2. The Mafic Complex

The Mafic Complex is a layered igneous intrusion of broadly gabbroic composition that was emplaced between 286 and 282 Ma (Guergouz et al., 2018; Henk et al., 1997; Karakas et al., 2019; Peressini et al., 2007), although gabbroic magmatism in the IVZ is present as dikes and sills as old as ~315 Ma (Klötzli et al., 2014). It is exposed along the length of the IVZ, and its thickness varies from hundreds of meters to ~10 km in Val Sesia (Figure 1; Garuti, 1980). Quick et al. (2003) subdivided the intrusion into units dominated by amphibole gabbro, gabbro and norite, and diorite. Metasedimentary septae in the Mafic Complex preserve mineral assemblages of antiperthitic plagioclase, garnet, quartz, ±sillimanite, ±rutile, ±graphite, ±corundum; these assemblages are indicative of ultra-high metamorphic temperatures (≤1,000°C; Quick et al., 1994; Sinigoi et al., 1996).

2.3. Geochronology of the Ivrea-Verbano Zone

Siliciclastic metasediments in the IVZ contain prismatic, ≤2.0 Ga detrital zircon grains interpreted to have been derived from calc-alkaline igneous rocks (Ewing et al., 2013; Guergouz et al., 2018; Kunz et al., 2018; Peressini et al., 2007; Vavra et al., 1996; Vavra & Schaltegger, 1999). The youngest zircon cores have U-Pb dates between ~389 Ma and ~352 Ma (Kunz et al., 2018; Vavra et al., 1996; Vavra & Schaltegger, 1999), implying that sediment deposition was underway by ~350 Ma at the latest and continued until the onset of regional metamorphism at ~316 Ma (Ewing et al., 2013). Regional amphibolite-to granulite-facies metamorphism—the source of the extant metamorphic field gradient—initiated at 316 ± 3 Ma (zircon U-Pb dates; Ewing et al., 2013), predating the main intrusive phase of the Mafic Complex (~285 to 282 Ma; Karakas et al., 2019) by 28–37 Ma. However, Klötzli et al. (2014) reported zircon U-Pb dates from the gabbroic Monte Capio sill of 314 ± 5 Ma, showing that the regional metamorphic event was contemporaneous with local mafic igneous activity.

The regional thermal climax occurred either during or after construction of the IVZ crustal section, but there is little consensus regarding the heat source. Conductive heating associated with intrusion of the Mafic Complex can only explain the most recent high-T event, as it produced a 2 km-wide low-*P* metamorphic aureole with cordierite, hercynite, and andalusite that texturally overprinted the earlier, higher-*P* amphibolite-to granulite-facies metamorphism (Barboza & Bergantz, 2000; Barboza et al., 1999; Quick et al., 1994; Schaltegger & Brack, 2007; Snoke et al., 1999; Zingg et al., 1990). Peak contact metamorphic temperatures of 900°C–910°C were reached shortly after emplacement of the Mafic Complex, and were followed by ~100°C–200°C of cooling by 284 ± 3 Ma and a further ~60°C–100°C cooling by 259 ± 3 Ma (Ewing et al., 2015; Peressini et al., 2007).

The post-Permian (290–180 Ma) history of the IVZ was characterized by conductive cooling interspersed by brief episodes of magmatic heating and hydrothermal activity (Ewing et al., 2015; Siegesmund et al., 2008; Smye et al., 2019; Vavra et al., 1996; Vavra & Schaltegger, 1999). Local, late, small-volume magmatic activity has been documented along the entire IVZ (Denyszyn et al., 2018; Galli et al., 2019; Zanetti et al., 2013). This record of spatially restricted magmatism throughout the Triassic-Jurassic was accompanied by widespread hydrothermal recrystallization of zircon and monazite, yielding U–Pb dates from ~260 Ma to ~200 Ma (Ewing et al., 2013;

Table 1
Summary of Mineral Assemblages and Peak PT Estimates for the Metapelitic Samples Investigated

Sample	Location	Major Phases[a]	Accessory Phases	P (kbar)	T (°C)
Lower amphibolite-facies metapelites (Kinzigites)					
MW23	N45.897563° E8.383018°	pl-bt-ms-fi(sil)-qz	ilm-mnz-zrn		
MW25	N45.901280° E8.371999°	pl-bt-qz	ilm-mnz-zrn		
MW20	N45.903929° E8.373885°	pl-bt-qz	ilm-mnz-rt-zrn-xtm		
MW19	N45.904450° E8.357558°	gt-pl-bt-ms-fi(sil)-qz	ilm-mnz-zrn	<6	<675
Upper amphibolite-facies metapelites (Kinzigites)					
MW04	N45.908236° E8.348736°	gt-pl-kfs-bt-fi(sil)-qz	ilm-mnz-rt-zrn	7.6–8.5	730–775
MW03	N45.907703° E8.336062°	gt-pl-kfs-bt-ms-fi(sil)-qz	ilm-mnz-rt-zrn	6.8–7.1	680–720
AS22	N45.907703° E8.336062°	pl-kfs-bt-ms-fi(sil)-qz	ilm-mnz-rt-zrn	<6.9	<675
MW02	N45.907703° E8.336062°	gt-pl-kfs-bt-ms-fi(sil)-qz	ilm-mnz-rt-zrn		
Granulite-facies metapelites (Stronalites)					
AS13	N45.930966° E8.291926°	gt-pl-kfs-bt-pris(sil)-qz	ap-ilm-mnz-rt-ttn-zrn	7.1–10.5	790–830
AS07	N45.936811° E8.274740°	gt-pl-kfs-pris(sil)-qz	ap-ilm-mnz-rt-ttn-zrn	8.1–11	810–860
AS06	N45.934170° E 8.267480°	gt-kfs-pris(sil)-qz	ap-ilm-mnz-rt-ttn-zrn	>8.2	>860

[a]fib(sil) and pris(sil) denote fibrous and prismatic sillimanite, respectively.

Guergouz et al., 2018; Vavra et al., 1996; Vavra & Schaltegger, 1999). Despite textural equilibration during the Permian high-temperature event, rutile U-Pb dates span ~220 to ~150 Ma (Ewing et al., 2015; Smye et al., 2019; Smye & Stockli, 2014) implying further diffusive resetting during Tethyan rifting. Combined, these constraints support the interpretation that the IVZ underwent episodic magmatic heating and metasomatism in response to mantle thinning following emplacement of the Mafic Complex (Ewing et al., 2013; Morishita et al., 2008; Smye et al., 2019).

3. Sample Petrography

We performed a dense sampling transect along Val Strona di Omegna, a 20 km long, NW-SE trending river valley that exposes the widest portion of the IVZ section (Figure 1a). Here, we focus on a subset of 11 metapelite samples (Figure 1b) selected according to the following criteria: (a) the presence of abundant dateable monazite, (b) the absence of pervasive retrograde metamorphic phases and fabrics, and (c) structural position along the Val Strona di Omegna transect. Samples are classified as belonging to the amphibolite- or granulite-facies according to peak metamorphic paragenesis, listed in Table 1.

3.1. Amphibolite-Facies Samples (Kinzigites)

Amphibolite-facies metapelites are categorized into those belonging to the lower and upper amphibolite facies. The lower amphibolite-facies metapelites MW19, MW20, MW23 and MW25a contain quartz + plagioclase + ilmenite + biotite ± muscovite ± fibrous sillimanite ± K-feldspar ± rutile ± garnet with accessory monazite, zircon, apatite, and rare xenotime. Of the four lower amphibolite-facies metapelites investigated, only MW19 contains garnet and has scarcer, smaller garnets than upper amphibolite-facies metapelites (Figures 2a and 2d); these garnet crystals occur as small hypidioblastic crystals between 0.2 and 1 mm in diameter. Garnet inclusions are predominantly quartz and minor oxides, and are mostly restricted to core domains. In samples MW19 and MW23, fibrous sillimanite forms rafts <2 mm in diameter associated with biotite and, less commonly, muscovite. Together, biotite, muscovite and fibrous sillimanite define a schistosity that is more pronounced than in higher-grade samples; outcrops are highly fissile, and hand samples and thin sections feature prominent 1–2 mm-wide bands of micas separating quartzofeldspathic segregations (Figure 2a).

Upper amphibolite-facies samples MW02, MW03, MW04 and AS22 contain quartz + plagioclase + K-feldspar + fibrous sillimanite + ilmenite + garnet + muscovite + rutile with accessory monazite, zircon and apatite

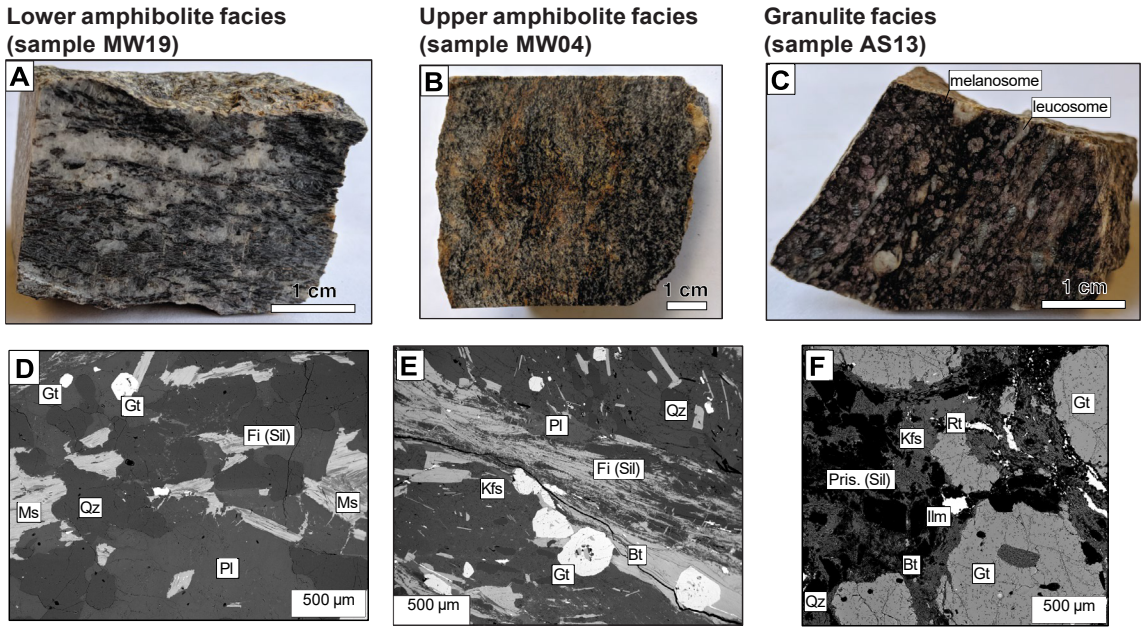

Figure 2. Sample petrography. (a–c) photographs of hand-specimens of lower and upper amphibolite-facies and granulite-facies samples from Val Strona di Omegna; (d–f) Backscattered electron images of the hand specimens directly above. (a), (d) muscovite and biotite-rich schist (MW19) with mats of fibrous sillimanite enveloping small (<300 μm) garnet porphyroblasts. (b), (e) fine-grained, biotite-rich schist (MW04); sillimanite is predominantly fibrolite and muscovite is subordinate to biotite. (c, f) garnet-rich, residual granulite (AS13) from the base of Val Strona di Omegna. Note the presence of rutile compared to lower-grade samples and the biotite-rich and quartz + plagioclase-rich melanosomes and leucosomes, respectively; sillimanite is predominantly prismatic. Mineral abbreviations after Whitney and Evans (2010).

(Figures 2b and 2e). These metapelites are distinguishable from their lower-grade counterparts by the prevalence of biotite over muscovite, more abundant garnet, K-feldspar and fibrolitic sillimanite, and an intense crenulation of the pervasive micaceous foliation. Rounded, poikiloblastic garnet crystals between 0.5 and 3 mm in diameter are spatially associated with leucocratic seams of quartz and plagioclase, and contain inclusions of quartz with minor oxides, rutile and sillimanite.

Monazite is common throughout the amphibolite-facies samples, principally as small (<200 µm diameter) subhedral to anhedral grains situated on grain boundaries between matrix biotite, quartz, muscovite and feldspar (Figure 3). Monazite inclusions in garnet are rare; sample MW23—the shallowest sample investigated—contains a single included grain. We do not observe the systematic decrease in monazite grain size within increasing metamorphic grade that was noted by Bea and Montero (1999). Amphibolite-facies monazite is generally characterized by irregular, patchy Y zonation with the majority of grains exhibiting Y-rich rims (Figure 4). Monazite from sample MW20 is an exception and is characterized by lower Y concentrations and an absence of intragrain zonation.

3.2. Granulite-Facies Samples (Stronalites)

Granulite-facies metapelites (samples AS06, AS07, AS13) are metatexites, comprising leucosome domains (10–20 vol.%) of quartz, large, anhedral K-feldspar blasts (up to 6 mm), plagioclase, and prismatic sillimanite, within melanosomes (1–2 cm wide) dominated by garnet, rutile, ilmenite and minor biotite + muscovite (Figures 2c and 2f). The boundaries between the leucosomes and melanosomes become more sharply defined with increasing structural depth (see also Carvalho et al., 2019). Garnet in samples AS07 and AS13 occurs as idio-to hypidioblastic poikiloblasts ranging in size from 0.4 to 5 mm in diameter, whereas garnet in the structurally deepest sample (AS06) is xenoblastic and occurs as 2–3 mm bands that alternate with prismatic sillimanite-rich domains. Included phases in garnet are predominantly quartz and sillimanite, with subordinate rutile and biotite. Monazite occurs as rare included grains within garnet and, more commonly, along grain boundaries of major phases (Figures 3c and 3d). Monazite inclusions and a minor proportion of matrix monazite grains exhibit similar habits and Y-zonation to amphibolite-facies monazite, comprising irregular grain boundaries and patchy

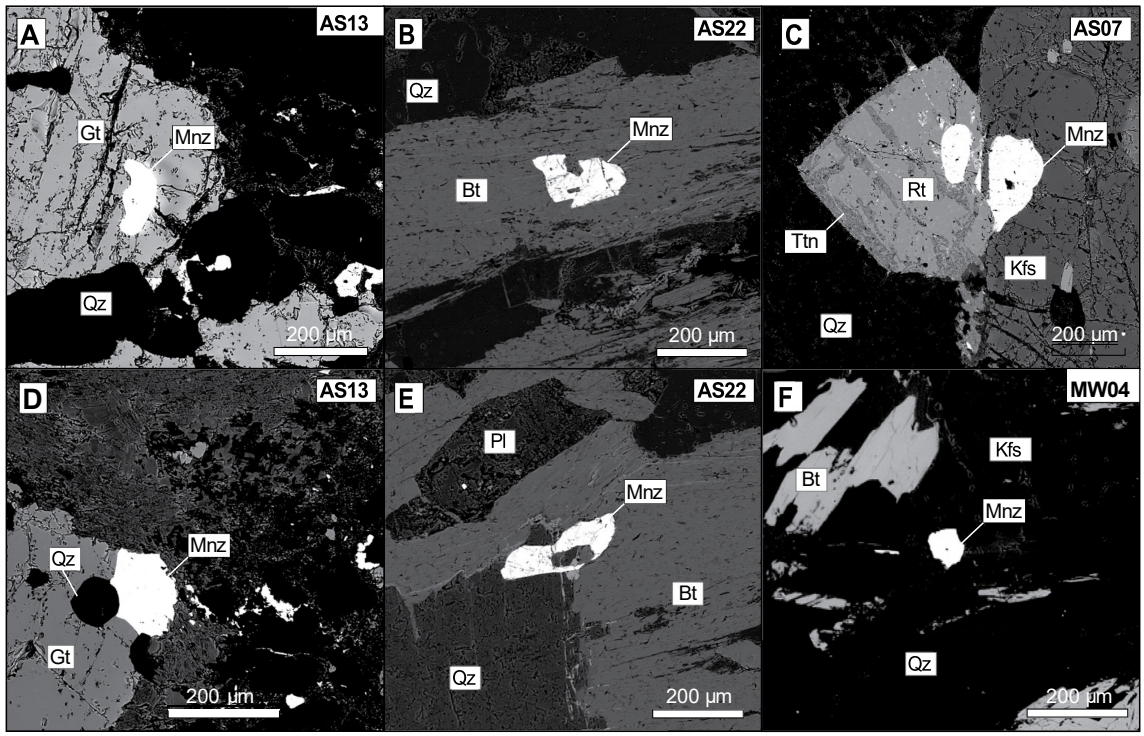

Figure 3. Backscattered-electron images of monazite textures along Val Strona di Omegna. Panel (a) anhedral monazite included in garnet, monazite 7, AS13; (b) anhedral monazite included in matrix biotite, monazite 6b, AS22; (c) rounded monazite grains included in rutile and K-feldspar blasts, sample AS07; (d) monazite partially included in garnet, monazite 4, sample AS13; (e) monazite partially included in matrix quartz and biotite, monazite 6a, sample AS22; (f) matrix monazite (monazite 3), sample MW04.

Y distributions (Figure 4). The majority of matrix monazite, however, is characterized by rounded to sub-angular grain morphologies and homogenous Y zonation (e.g., sample AS07, Figure 4), and are typically associated with sillimanite, K-feldspar and quartz.

4. Pressure-Temperature Conditions

To link monazite U-Th-Pb dates and trace element (TE) compositions to pressures (P) and temperatures (T) of formation, we calculated a series of PT pseudosections that span 3–12 kbar and 600°C–950°C, for key monazite-bearing samples. These PT estimates (Figure 5) are quantitatively similar to existing estimates of the Permian metamorphic field gradient along Val Strona di Omegna (see Section 2.1). All calculations were undertaken in the simplified chemical system MnO –Na_2O –CaO– K_2O – FeO–MgO– Al_2O_3– SiO_2–H_2O– TiO_2–O (MnNCKFMASHTO) using Theriak-Domino (De Capitani & Brown, 1987) with the Holland and Powell (1998) database

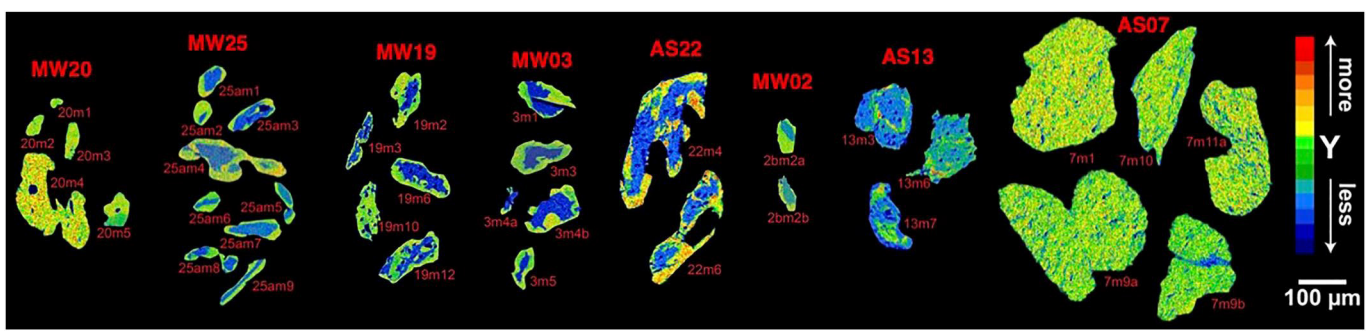

Figure 4. Monazite size, morphology and yttrium zonation along Val Strona di Omegna. Panel shows Y maps for multiple monazite grains from samples arranged in order of increasing metamorphic grade, from left-to-right.

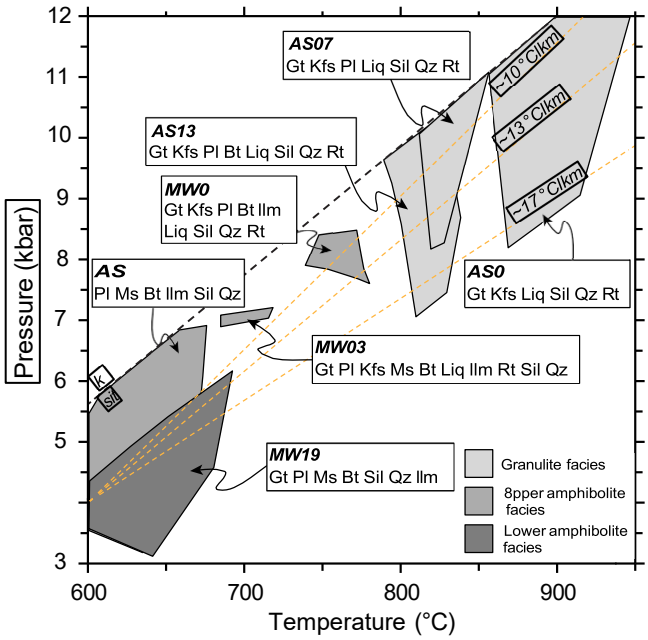

Figure 5. Summary of the inferred peak pressure-temperature (*PT*) conditions for monazite-bearing samples along Val Strona di Omegna. Polygons correspond to *PT* stability fields of peak mineral parageneses derived from pseudosection calculations. Dashed lines represent metamorphic field gradients. See text for discussion.

(ds55) and the following activity-composition models: biotite, garnet and melt (White et al., 2007), cordierite, chloritoid and epidote (Holland & Powell, 1998), muscovite (Coggon & Holland, 2002), plagioclase and alkali feldspar (Holland & Powell, 2003), magnetite and orthopyroxene (White et al., 2002), chlorite (Mahar et al., 1997; Holland et al., 1998), clinopyroxene (Green et al., 2007) and ilmenite, hematite, and low grade magnetite (White et al., 2000). The calculations used X-Ray Fluorescence (XRF) bulk compositions with H_2O values derived from bulk loss on ignition (LOI) values and a fixed bulk Fe_2O_3 value of 0.1 mol.% following Redler et al. (2012). Bulk compositions used for modeling and the resultant peak *PT* estimates are presented in Table 2. Peak metamorphic *PT* conditions were constrained using the inferred peak mineral assemblage for each sample (Figure 5). We avoided the use of phase compositions for thermobarometry because granulitic phases typically undergo post-peak chemical re-equilibration (e.g., Frost & Chacko, 1989; Pattison et al., 2003). A summary of the peak *PT* stability fields is presented in Figure 5 and salient results are presented below.

The primary constraints on maximum and minimum metamorphic pressures by metapelitic phase relations along Val Strona di Omegna are the presence of sillimanite, not kyanite, and the absence of spinel. Peak temperatures are constrained by phase relations among muscovite, biotite, plagioclase, K-feldspar and melt. In lower amphibolite-facies metapelites, coexisting muscovite and biotite and the absence of abundant K-feldspar + rutile constrains peak conditions to <700°C at <6 kbar. Garnet-absent phase assemblages are not predicted in pseudosections for samples MW20 and MW25a, implying that either garnet was consumed during decompression, or that the MnO concentration of the XRF bulk does not accurately represent the effective bulk composition. The presence of K-feldspar, garnet and coexisting muscovite and biotite in upper amphibolite-facies metapelites constrains peak *PT* conditions to ~6.8 to 8.5 kbar at <775°C. Specifically, the absence of garnet in sample AS22—located <200 m from samples MW02 and MW03—imposes a broad range of peak *PT* conditions that are notably similar to those derived from lower amphibolite-facies sample MW19, located ~1.5 km up-section. This apparent inconsistency in the progressive field gradient along Val Strona di Omegna could be explained by the consumption of garnet during post-peak retrogression or by late structural juxtaposition of these samples. Each of the granulite-facies metapelites experienced peak temperatures

Table 2
XRF Bulk-Rock Compositions (wt.%)

	MW25	MW20	MW19	MW04	AS22	MW03	AS13	AS07	AS06
SiO_2	62.37	62.90	56.29	53.71	54.96	51.81	57.27	49.52	46.92
TiO_2	0.90	0.83	1.27	1.18	1.24	1.38	1.41	2.60	1.92
Al_2O_3	15.96	17.45	22.80	25.41	24.34	23.04	20.75	21.66	26.91
Fe_2O_3[a]	8.65	4.93	10.22	8.44	10.76	14.12	11.43	14.31	16.18
MnO	0.12	0.07	0.19	0.11	0.07	0.58	0.12	0.23	0.14
MgO	4.00	4.21	2.85	1.57	2.94	3.02	4.02	4.52	4.81
CaO	1.86	3.71	0.58	2.00	0.13	0.71	1.20	2.34	0.46
Na_2O	2.60	3.39	1.28	1.95	0.08	1.02	0.71	3.48	*bdl*
K_2O	2.99	2.54	4.04	5.37	3.89	3.87	2.53	0.90	1.94
P_2O_5	0.18	0.21	0.18	0.16	0.08	0.19	0.11	0.12	1.94
Total	99.63	100.24	99.70	99.90	98.49	99.74	99.53	99.66	99.29
LOI	1.87	1.30	2.26	2.06	1.51	2.73	0.47	0.34	0.71

[a]All Fe as Fe_2O_3; bdl is below detection limit.

in excess of the muscovite-out reaction that limits minimum *T* to ~800°C at >8.5 kbar. Finally, the absence of biotite and the presence of a ternary K-feldspar in sample AS06 provides a maximum *PT* constraint along the Val Strona field gradient of >8.2 kbar and >860°C.

The progressive increase in peak metamorphic *PT* conditions derived from monazite-bearing metapelites along Van Strona di Omegna defines a metamorphic field gradient between ~10 and ~17°C/km (calculated assuming a crustal density of 2,750 kg/m^3). Such a gradient is consistent with the modeled field gradient proposed for Val Strona di Omegna by Redler et al. (2012) (8–16°C/km) and Kunz and White (2019), as well as the regional pattern of increasing metamorphic grade toward the Insubric Line observed throughout the IVZ.

5. Analytical Methods

5.1. Electron Microscopy (SEM and EPMA)

All analyses were performed on polished thin sections to link U-Pb dates and TE concentrations to the monazite textural context within the sample. Monazite grains were identified, located and imaged using energy-dispersive spectroscopy and back scattered electrons on FEI Quanta 200 and FEI Quanta 250 scanning electron microscopes (SEMs) located in Pennsylvania State University's Materials Characterization Laboratory. Zoning in Y, Na, Ce, K, La, Sr, Mg, Nd, Ca, Th, Al, Si, U, P, and Fe in monazite was assessed qualitatively with X-ray maps on a Cameca SXFive electron probe microanalyzer (EPMA) at Penn State using an accelerating voltage of 20 keV, a beam current of 30 nA, a step size of 0.2 μm and a dwell time of 25 ms per spot. Quantitative analyses of garnet major-element compositions were conducted on the same instrument using an accelerating voltage of 15 keV, a beam current of 30 nA, and on-peak count-times of 10–30 s.

5.2. Monazite U-Th-Pb and Trace-Element Measurements by Laser Ablation Split Stream Inductively Coupled Plasma Mass Spectrometry (LASS-ICP-MS)

Monazite U-Pb and Th-Pb dates and TE abundances were analyzed at the UC Santa Barbara LASS-ICP-MS facility. All monazite grains were analyzed in thin sections so that the monazite U–Pb dates and trace-element abundances could be linked to specific metamorphic textures and parageneses, and U-Pb and trace-element data were collected simultaneously from the same spots. A Photon Machines 193 nm excimer laser and HelEx sample cell were used in connection with a Nu Plasma HR MC-ICPMS (U-Th-Pb isotopes) and an Agilent 7700S quadrupole ICPMS (TEs). The analyses were obtained with an 8 μm-diameter laser spot, using a frequency of 3 Hz, a 25 s ablation time, and a fluence of ~1–2 J/cm^2. Two cleaning shots were performed prior to each analysis; a ~15 s pause for washout was followed by 75 analytical shots, with a 20 s delay between analyses. Analyses of IVZ monazite grains were interspersed with analyses of the monazite reference standards 44069 (424.9 ± 0.4 Ma SHRIMP ^{206}Pb/^{238}U-^{207}Pb/^{235}U concordia age, Aleinikoff et al., 2006) and Stern (~512.1 ± 1.9 Ma ID-TIMS ^{206}Pb/^{238}U age, Palin et al., 2013); 44069 was the primary standard for U–Pb analyses and Stern was the primary standard for TE analyses. Monazites FC (55.7 ± 0.7 Ma ID-TIMS ^{206}Pb/^{238}U age, Horstwood et al., 2003), Trebilcock (272 ± 3.2 Ma ID-TIMS ^{207}Pb/^{235}U age, Tomascak et al., 1996), and Manangotry (555 ± 1.6 Ma ID-TIMS ^{206}Pb/^{238}U age, Horstwood et al., 2003) were used as secondary standards to monitor data accuracy. This investigation obtained mean ^{206}Pb-^{238}U dates of 512.7 ± 1.3 Ma for Stern, 56.8 ± 0.3 Ma for FC, 276.0 ± 1 for Trebilcock, and 562.1 ± 3.4 Ma for Manangotry; these ages are accurate to within 0.1%, 1.3%, 1.5%, and 1.9% of the reference values, respectively. ^{208}Pb-^{232}Th ratios for primary U-Pb standard 44,069 have not been determined by isotope dilution methods, but assuming U-Th-Pb isotopic concordance yields average ^{208}Pb-^{232}Th dates of 497.8 ± 7.1 Ma for Stern and 54.3 ± 0.4 Ma for FC-1, both within 2% uncertainty of published U/Pb dates; we obtained ^{208}Pb-^{232}Th dates of 256.1 ± 2.3 Ma for Trebilcock and 526.4 ± 4.5 Ma for Manangotry, but note that these reference materials are unreliable Th/Pb secondary standards (e.g., Horstwood et al., 2016; Kohn & Vervoort, 2008; Paquette & Tiepolo, 2007). Data reduction was performed using the Iolite plug-in v. 3.7 (Paton et al., 2011) for the Wavemetrics IgorPro software and U-Pb Concordia were plotted using IsoPlotR (Vermeesch, 2018). The U-Th-Pb data reduction strategy and common-Pb (Pb_c) correction procedure followed the methods in Garber et al. (2020). Due to the possibility of individual spot dates to be affected by analytical mixing between discrete chemical domains, our interpretation of monazite spot dates is concentrated on the average ages of statistically significant peaks identified using kernel density spectra and Gaussian deconvolution (Figure 6).

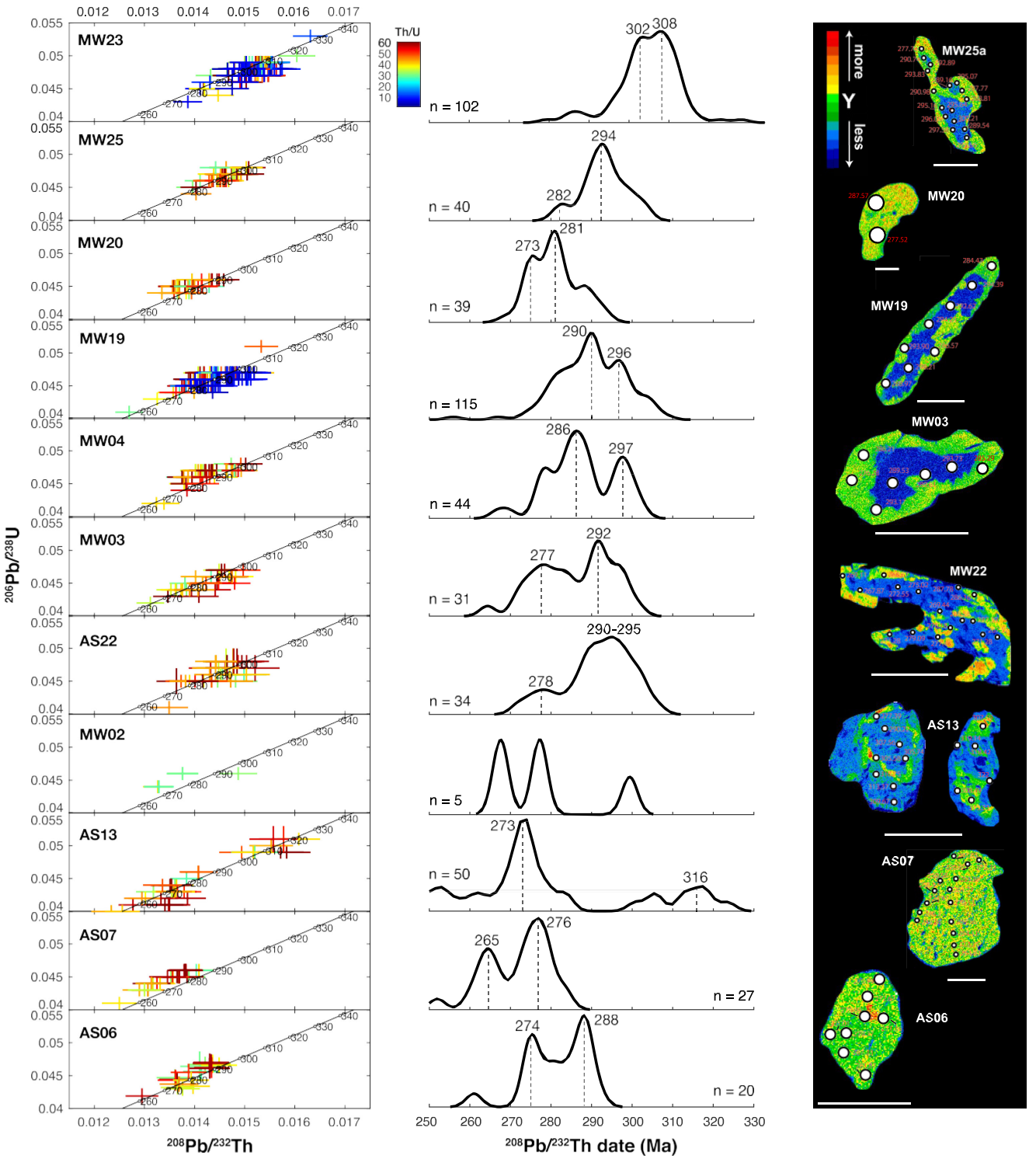

Figure 6. Monazite Th-Pb dates. From left to right, columns show individual analyses plotted on $^{208}Pb/^{232}Th$-$^{206}Pb/^{238}U$ concordia and shaded according to Th/U (error bars represent 2σ uncertainty), KDE's with labeled population peaks and spot date distributions superimposed on Y concentration maps of individual monazite grains (scale bars represent 100 μm). Each of these plots present ^{207}Pb-corrected $^{208}Pb/^{232}Th$ spot dates that are <5% discordant from $^{208}Pb/^{232}Th$-$^{206}Pb/^{238}U$ concordia.

5.3. Garnet Trace-Element Measurements by LA-ICP-MS

Laser-ablation inductively coupled plasma mass spectrometry (LA-ICPMS) for garnet TEs was performed at the LionChron facility at Penn State. Samples were ablated in thin section using a Teledyne/Photon Machines Analyte G2 excimer laser ablation system with a Helex2 ablation cell, coupled to a Thermo Scientific iCAP-RQ ICPMS system for TEs. The total Ar gas flow for the experiment was 1.01 L/min, with total He gas flows from the laser at 0.44 L/min. All samples were run during the same session, with a 35 μm spot, 10 Hz repetition rate, 300 shots, and a laser fluence at the sample surface of 3.66 J/cm^2, yielding pit depths on the order of ~10 to 15 μm. The laser was first fired thrice with the same spot size to remove surface contamination, and this material was allowed to wash out for 20 s. Analyses of unknowns were bracketed by analyses of whole-rock glasses from the Max-Planck-Institut (Jochum et al., 2006) spanning a range of major-element compositions, including Gorgona Island komatiite G128-G, Kilauea basalt KL2-G, Alpine quartz diorite T1G, and Mt. St. Helens andesite StHs6/80-G. T1G was used as the primary reference material for all analyses. For trace-element quantification, ^{27}Al (assuming ~11.5 wt. % Al, using an EPMA-based average) was used as an internal standard, with measured peaks on the iCAP-RQ at ^{29}Si, ^{31}P, ^{43}Ca, ^{45}Sc, ^{49}Ti, ^{51}V, ^{52}Cr, ^{59}Co, ^{66}Zn, ^{87}Sr, ^{89}Y, ^{90}Zr, ^{93}Nb, ^{139}La, ^{140}Ce, ^{141}Pr, ^{146}Nd, ^{147}Sm, ^{153}Eu, ^{157}Gd, ^{159}Tb, ^{163}Dy, ^{165}Ho, ^{166}Er, ^{169} Tm, ^{172}Yb, ^{175}Lu, ^{178}Hf, ^{181}Ta, ^{182}W, and ^{238}U. Iolite version 4 (Paton et al., 2011) was used to corrected measured isotopic ratios and elemental intensities for baselines, time-dependent laser-induced inter-element fractionation, plasma-induced fractionation, and instrumental drift. The mean and standard error of the measured ratios of the backgrounds and peaks were calculated after rejection of outliers more than two standard errors beyond the mean. Using the same methods as applied to unknowns, and treating all whole-rock glasses besides T1G as secondary reference materials, this routine yielded values accurate to within 5% for REE, 10% for HFSE and transition metals, and 20% for all other elements.

5.4. X-Ray Fluorescence

Bulk rock compositions were determined by XRF at Franklin and Marshall College using a Malvern PANalytical, Inc. Zetium XRF vacuum spectrometer. Difference in sample weight before and after heating to 950°C for 1.5 hr was used to determine LOI. All oxide uncertainties are <1%.

6. Results

6.1. Monazite U-Th-Pb and Trace Element Data

Monazite ^{208}Pb/^{232}Th dates are reported for all samples because these dates avoid any problems with thorogenic Pb on ^{206}Pb/^{238}U dates (Schärer, 1984) and because the presence of common Pb – albeit minor (Figure S1) – has a negligible effect on ^{208}Pb/^{232}Th ratios. However, we discarded all Pb_C-corrected ^{208}Pb/^{232}Th spot dates that are >5% discordant from ^{208}Pb/^{232}Th-^{206}Pb/^{238}U concordia. Individual Pb_C-corrected ^{208}Pb/^{232}Th monazite dates and TE concentrations obtained for each of the samples are provided in Table S1; raw Tera-Wasserburg plots and Pb_C-corrected ^{208}Pb/^{232}Th-^{206}Pb/^{238}U concordia plots are presented for each sample in Figure S1 and Figure 6, respectively. The data set is characterized by: (a) protracted intra-sample dispersion in Pb_C-corrected ^{208}Pb/^{232}Th spot dates, encompassing spreads of ~15 to 130 Myr; (b) a predominance of spot dates between 270 and 300 Ma, and (c) few dates older than 300 Ma.

Monazite isotopic data from lower amphibolite-facies samples spanning the uppermost ~3 km of Val Strona di Omegna (MW23, MW25a, MW20 and MW19) show a significant spread in monazite dates, from ~320 to ~240 Ma, the vast majority of which are concordant (Figure 6). The structurally shallowest sample (MW23) is the only sample with a significant fraction of Th-Pb dates >300 Ma (76/101); the 10 monazite grains analyzed yield a continuous range of dates spanning ~50 Myr, from 327 ± 7 Ma to 278 ± 6 Ma, and do not define a single age population (weighted mean age = 304.3 ± 0.3 Ma, MSWD = 2.8, n = 101). Notably, Th-Pb dates >300 Ma are preserved in matrix monazite grains. On a kernel density estimation (KDE) plot (Figure 6) these dates define two partially resolved peaks at ~308 and ~302 Ma, respectively, and a minor peak at ~285 Ma; as none of the peaks define a coherent population, we did not calculate weighted mean ages. Sample MW25a yields a spread of concordant spot dates between 303 ± 7 and 280 ± 7 Ma (weighted mean age = 292 ± 1 Ma, MSWD = 2.7, n = 40). On a KDE plot these dates define a major peak with a weighted mean age of 294 ± 1 Ma (MSWD = 1.4, n = 30) and a minor peak at ~282 Ma. For sample MW20, dates spread between 293 ± 7 Ma and 268 ± 6 Ma (weighted mean age = 280 ± 1 Ma, MSWD = 3.4, n = 39); partially resolved KDE peaks are present at ~281 Ma

and ~273 Ma. Dates from sample MW19 span ~50 Myr, from 307 ± 7 to 255 ± 6 Ma and the majority of dates are <300 Ma (94/104). The KDE spectrum for these dates is characterized by a prominent peak with a weighted mean age of 290 ± 1 Ma (MSWD = 0.6, n = 49/104) and a partially resolved peak at 296 Ma (Figure 6).

These lowest-grade monazite grains show a systematic compositional variation with spot date. Chondrite-normalized REE patterns (REE_N) from samples MW23, MW20 and MW19 define a trend of higher heavy rare earth element ($HREE_N$) values with decreasing age (Figure S2); Y concentrations are <2.5 wt.% and define a similar trend, with the lowest concentrations corresponding to older spot dates (Figure S3). These data are consistent with monazite Y maps from samples MW19 and MW25 that exhibit discrete low-Y cores surrounded by high-Y mantles (Figures 4 and 6). Spot dates from each domain correspond to the two dominant age peaks recognized in the KDE plots (Figure 6). Eu/Eu* also decreases with decreasing spot dates in monazite arrays from each of the samples, albeit with more scatter than the Y data (Figure S4). Arrays of Th/U are characterized by significant dispersion in Th/U from 0.8 to 9.5, but the data do suggest a general increase from minimum values of at ~300 Ma to higher values by 285 Ma; this trend is particularly apparent in monazite from sample MW25a (Figure S5).

Upper amphibolite-facies samples MW02, MW03, MW04 and AS22 exhibit a similar spread in Pb_C-corrected $^{208}Pb/^{232}Th$ dates to the lower amphibolite-facies samples. Sample MW04 yields an array of concordant spot dates between 301 ± 7 and 265 ± 6 Ma that do not conform to a single population (weighted mean age = 287 ± 1 Ma, MSWD = 5.7, n = 43). Gaussian deconvolution confirms the ages of two well-defined KDE peaks at 297 ± 1 Ma (MSWD = 0.3, n = 11) and 286 ± 1 Ma (MSWD = 0.4, n = 19), and a partially resolved peak at ~278 Ma. Sample MW03 yields concordant spot dates between 300 ± 7 and 263 ± 6 Ma (weighted mean age = 285 ± 1 Ma, MSWD = 7.3, n = 30), with a dominant age peak at 292 ± 1 Ma (MSWD = 0.86, n = 14) and a subordinate peak at 277 ± 1 Ma (MSWD = 0.99, n = 11). Sample AS22, exhibits a protracted spread in concordant ^{207}Pb-corrected $^{208}Pb/^{232}Th$ dates between 305 ± 10 and 270 ± 8 Ma (weighted mean age = 289 ± 1 Ma, MSWD = 4.3, n = 33) that define a KDE spectrum with a broad age peak at 295-290 Ma and a minor peak at 278 ± 1 Ma (MSWD = 1.66, n = 8). The small number of concordant dates (n = 5) from sample MW02 range between 298 ± 8 and 266 ± 6 Ma and preclude any meaningful statistical analysis.

Values of REE_N, Eu/Eu* and Th/U from the upper-amphibole facies monazite defines similar temporal trends to monazite from the lower amphibolite-facies samples. In particular, monazite from samples MW04 and AS22 exhibit well-defined increases in Y (<0.5 wt.% ~300 Ma to ~2 wt.% at ~280 Ma) and $HREE_N$ values and a concomitant decrease in Eu/Eu* with decreasing spot date. Th/U ranges from 0.5 to 17.4 in all samples within this sub-group; sample MW02 is the only sample to yield a resolvable decrease in values, from peak Th/U of ~6.5 at ~298 Ma, to <4 by ~262 Ma.

Monazite from granulite-facies samples AS06, AS07 and AS13 yield a protracted spread of ^{207}Pb-corrected $^{208}Pb/^{232}Th$ dates with almost uniformly younger ages than amphibolite-facies monazite. In order of increasing structural depth: sample AS13 exhibits the greatest spread in monazite spot dates of the entire data set, from 322 ± 9 to 186 ± 6 Ma, and yields a complex KDE spectrum defined by a dominant age peak at 273 ± 1 Ma (MSWD = 1, n = 18) and a minor but statistically significant peak at 316 ± 2 Ma, (MSWD = 0.8, n = 6). This older monazite population is defined by a majority of spot analyses from a monazite grain included within garnet (monazite grain VII; Figures 3a and 4). Sample AS13 also yields a small group of concordant spot dates that give a mean age of 197 ± 1 Ma (MSWD = 0.1, n = 5). Concordant monazite spot dates from sample AS07 spread between 283 ± 7 and 251 ± 7 Ma and define a KDE spectrum with a well-resolved and dominant age peak at 276 ± 1 Ma (MSWD = 1.0, n = 17) in addition to a minor peak at 265 ± 1 Ma (MSWD = 1.0, n = 9). Sample AS06, the highest-grade sample investigated, has a continuum of spot dates from 291 ± 7–260 ± 7 Ma with two KDE peaks; the strongest age peak has a weighted mean age of 288 ± 1 Ma (MSWD = 0.2, n = 9) and a partially resolved peak is present at ~274 Ma.

Monazite from granulite-facies samples has significantly elevated Th/U (majority of analyses have Th/U between 20 and 166) and lower Y concentrations (<0.4 wt.%) and Eu/Eu* (<~0.5) compared to amphibolite-facies monazite. Sample AS13 preserves a temporal variation in monazite composition defined by a progressive increase in $MREE_N/HREE_N$ and Th/U, and decreasing Y concentration and Eu/Eu* with decreasing spot date (Figures S2–S5). This progression in HREE concentrations is opposite to that observed in amphibolite-facies monazite. There is no resolvable temporal variation in TE concentrations in monazite from samples AS07 and AS06.

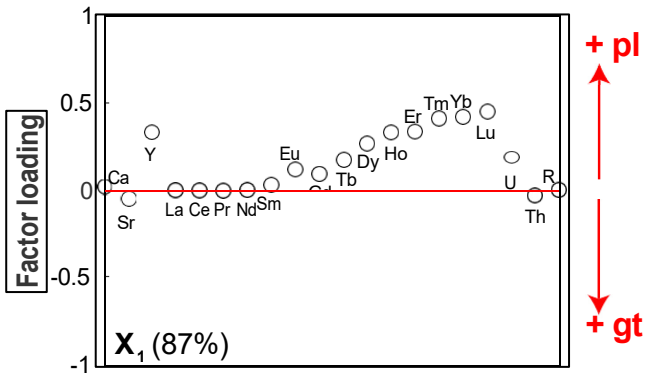

Figure 7. Trace element (TE) weightings on the dominant principal component (X_1). Red line corresponds to a zero weighting. Strong positive weightings for the MREE + HREE and Y, implies that monazite with elevated X_1 scores equilibrated under the influence of cogenetic plagioclase; in contrast, analyses with negative X_1 scores imply the influence of garnet on TE composition. See text for further discussion.

6.2. Garnet Major and Trace Element Compositions

Major element concentrations were collected from garnet from three samples that span the entire range of metamorphic grades: MW19 (lower amphibolite facies), MW04 (upper amphibolite facies) and AS13 (granulite facies). TE concentrations were collected from these three samples, as well as sample MW03. The raw major and TE concentration data are presented in Table S2 and Table S3, respectively, and trace-element data are displayed in Figures S6–S9.

Garnet from sample MW19 is principally an almandine-spessartine solid solution. Individual porphyroblasts are homogenous with respect to Fe, Mg and Mn, but exhibit core domains with maximum Ca concentrations ($alm_{70}sps_{20}prp_8grs_2$) surrounded by a low-Ca mantle ($alm_{71}sps_{22}prp_5grs_1$). Y and HREE concentrations conform to a similar pattern of zonation as Ca, defined by enriched core domains, low-concentration mantles and thin, high-Y rims (Figure S6). Garnet from sample MW04 is homogenous in major elements ($alm_{81}spss_8py_6gr_5$), but exhibits complex TE zonation (Figure S7). Y + HREE concentrations display three distinct zones: small (<100 μm diameter) core domains with 200–400 ppm Y that smoothly transition into lower-Y mantles (<200 ppm) that, in turn, are surrounded by high-Y + HREE rims (400–600 ppm Y). Garnet from sample MW03 displays core domains with internally homogenous Y + HREE concentrations (200–250 ppm Y), surrounded by high-Y + HREE annuli (250–350 ppm Y; Figure S8). Garnet from granulite-facies sample AS13 displays homogeneous major element zonation ($alm_{63}py_{33}gr_3spss_1$) and bell-shaped core-to-rim Y + HREE concentration profiles that are surrounded by thin (<50 μm), high-Y + HREE rims (200–250 ppm Y; Figure S9).

7. Principal Components Analysis of Monazite Composition

To identify temporal trends in monazite chemistry and the geological processes responsible for them, we reduced the dimensionality of the aggregate monazite trace-element data set (n = 427) with a principal components analysis (PCA; Aitchison, 1983). PCA is a basic ordination method that is particularly useful for trace-element data, as it facilitates the examination of intercorrelated trends among all measured elements simultaneously. Raw TE concentrations were transformed using a centered log-ratio transformation, and a constant-sum constraint was imposed by addition of a residual for each sample (see also Garber et al., 2017); the PCA was performed using the princomp function in MATLAB®.

The PCA reveals two principal components that collectively explain >90% of the total variance of the data set. The first principal component, X_1, accounts for ~87% of the total variance and is thus the dominant signal in the data set. Figure 7 presents the factor loadings of the standardized TEs for X_1 and shows that monazites with high X_1 scores are correlated with higher Y + MREE + HREE + U (Figure S10), whereas lower X_1 scores are correlated with higher Sr and Th abundances as well as slightly more negative Eu anomalies. These elemental groupings broadly describe the role of garnet (Y + MREE + HREE) and plagioclase (Eu/Eu*), and thus we interpret X_1 as a proxy for the coexistence of garnet or plagioclase at the time of monazite equilibration. We note, however, that additional phases influenced the composition of monazite from granulite-facies samples AS07 and AS13 that exhibits a positive correlation between Eu/Eu* and X_1 scores, in contrast to amphibolite-facies samples in which monazite Eu/Eu* and X_1 are anticorrelated, as expected if monazite chemistry is controlled predominantly by plagioclase/garnet modes (Figures S10 and S11). As the rocks investigated generally lack xenotime but contain apatite, we assume that Y + MREE + HREE(+P) partitioning between garnet, plagioclase and monazite occurred by the net-transfer reaction identified by Pyle et al. (2001):

$$Y_3Al_2Al_3O_{12}(YA-\text{garnet}) + Ca_5(PO_4)_3(OH)(OH-\text{apatite}) + 25/4SiO_2 = 5/4Ca_3Al_2Si_3O_{12}(Ca-\text{garnet}) + 5/4CaAl_2Si_2O_8(Ca-\text{plagioclase}) + 3YPO_4(Y-\text{monazite}) + 1/2H_2O \quad (1)$$

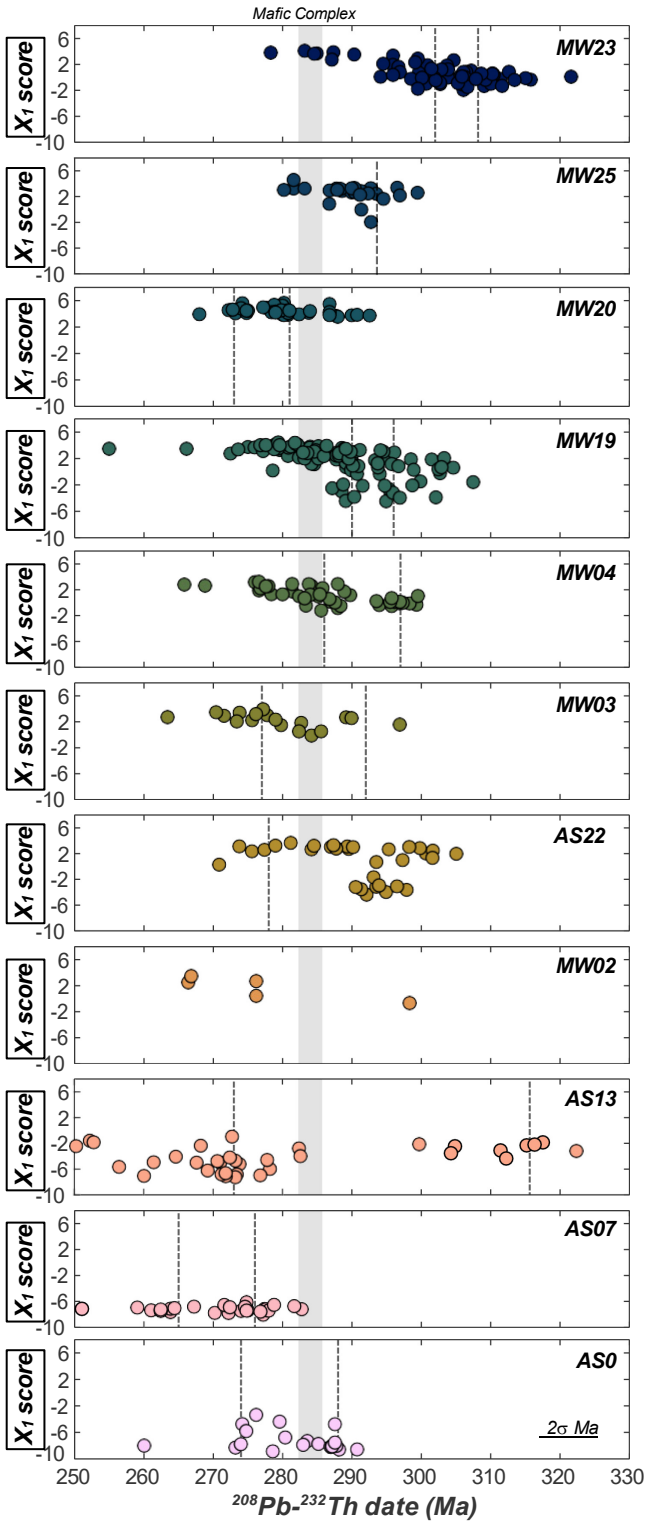

Figure 8. Sample X_1 scores versus Th-Pb spot dates. From top-to-bottom, sample data plots are arranged in order of increasing peak metamorphic grade and structural depth. Shaded gray bar represents the timing of emplacement of the Mafic Complex (286-282 Ma, Karakas et al., 2019); dashed lines correspond to the KDE age peaks identified in Figure 6. Typical error bar for ^{208}Pb-^{232}Th spot dates shown for reference.

Under this scheme, monazite analyses with high X_1 scores represent growth under "garnet-poor, plagioclase-rich" conditions—leading to higher monazite HREE concentrations —and vice versa. As the second principal component, X_2, accounts for only ~5% of the total variance, it is statistically insignificant above random, implying that variation in IVZ monazite TE composition almost solely reflects the competing roles of garnet and plagioclase.

8. Monazite Age Interpretation

Figure 8 shows the variation of X_1 score with ^{207}Pb-corrected ^{208}Pb-^{232}Th date for individual monazite spot analyses from each of the samples considered. Arranged in order of increasing structural depth, this presentation of the PCA results illustrates both intra- and inter-sample variations of the magnitude and timing of plagioclase/garnet influence on monazite chemistry. Inspection of the figure reveals a primary difference in the distribution of X_1 scores between the amphibolite- and granulite-facies samples, consistent with the smaller grain sizes, subhedral grain morphologies and distinct chemical zonation of amphibolite-facies monazite.

8.1. Amphibolite-Facies Monazite

Monazite data from six of the eight amphibolite-facies samples define a curvilinear increase in X_1 score from variable minimum values to a maximum of ~6. The core-rim Y zonation observed in monazite grains from samples MW25a, MW19, MW03 and AS22 imply that this trend is caused by analytical mixing of core and rim domains characterized by low and high X_1 scores, respectively. This interpretation draws support from plots of Y versus Eu/Eu* (Figure S11) on which spot dates for samples MW23, MW25a, MW19 and MW04 broadly decrease along a linear array between end-members with high-/low-Eu/Eu* and low-/high-Y. Accordingly, we interpret the age of the oldest resolvable KDE peak for each of these samples to represent the timing of monazite core growth. Such core growth ages broadly decrease with increasing structural depth from 308 to 302 Ma for MW23, 296 Ma for MW19, 292 Ma for MW03 to 290–295 Ma for AS22; samples MW19 (296 Ma) and MW04 (297 Ma) represent exceptions to this trend.

The low-X_1 scores and elevated Eu/Eu* values characteristic of monazite core domains are consistent with the interpretation that core growth occurred under garnet-present conditions. As garnet primarily grew in IVZ metasediments according to the reaction (Schmid & Wood, 1976):

$$\text{biotite} + \text{plagioclase} + \text{sillimanite} + \text{quartz} = \text{garnet} + \text{K} - \text{feldspar} + \text{rutile} + \text{melt},$$

It is reasonable to interpret that this monazite population equilibrated under suprasolidus conditions, consistent with the observation that monazite cores from samples MW23 and AS22 exhibit weakly oscillatory bands and sectors that are common to melt-derived monazite (e.g., Hermann & Rubatto, 2003; Rubatto et al., 2013; Vavra & Schaltegger, 1999). The absence of concordant monazite dates >330 Ma indicates that any detrital or inherited monazite that may have been present during prograde metamorphism was consumed, presumably through interactions with a melt/fluid phase. Such an inference is supported by the elevated solubility of monazite in granitic melts at metamorphic conditions relevant to the amphibolite-facies portion of the IVZ; for example, the solubility expression of Stepanov et al. (2012) predicts that a

granitic melt can dissolve >200 ppm LREE at 750°C at 7 kbar, exceeding typical bulk-rock values for kinzigites, between ~140 and 200 ppm (n = 3, data from Bea & Montero, 1999). Of course, whether this results in partial or complete monazite dissolution is dependent on the degree of partial melting. It is worth noting that subsolidus metamorphic fluids have also been shown to dissolve inherited and detrital monazite during prograde metamorphism (e.g., Harlov et al., 2011; Rasmussen & Muhling, 2007).

The elevated X_I scores preserved by high-Y monazite rim domains imply equilibration under a stronger(/weaker) influence of plagioclase(/garnet) relative to core domains. Given the inverse correlation of garnet and plagioclase modes in these samples with P and T, this can broadly be termed an "exhumation trend". Based on a broad correlation between spot position and date (Figure 6), we interpret the youngest resolvable KDE peak for each sample as recording the timing of rim growth; such ages span ~17 Myr, from 290 Ma for MW19, to 273 Ma, for MW20. The scalloped and lobate shape of core-rim boundaries, combined with the idiomorphic habit of monazite rims (Figure 4) is indicative of monazite (re)crystallization during a fluid-mediated dissolution-precipitation process (e.g., Putnis & Putnis, 2007). This process must have operated in an environment in which HREE and Y were readily available to the growing or recrystallizing monazite rims.

8.2. Granulite-Facies Monazite

Monazite from the three granulite-facies samples AS13, AS07 and AS06 are anhedral, largely unzoned in Y and yield major age components that are similar to the age of monazite rims from amphibolite-facies samples, indicating progressive replacement of prograde and/or peak monazite across the amphibolite-to-granulite-facies transition. The composition of granulite-facies monazite has two distinct characteristics relative to amphibolite-facies monazite: (a) elevated Th/U, implying that monazite crystallized from a zircon-saturated melt (e.g., Rubatto et al., 2006), and (b) a restricted range of low X_I scores, generally between −2 and −6, and a more muted dependence on spot date (Figure 8), consistent with co-crystallization of monazite and garnet over a protracted time period (288–265 Ma) that spans emplacement of the Mafic Complex. It is interesting to also note that the "exhumation trend" documented in amphibolite-facies monazite is not apparent in monazite from the granulite-facies samples.

Monazite from sample AS13 is particularly notable as spot analyses from an included monazite grain within garnet (monazite VII) and core domains of a matrix grain (monazite III) yield the oldest coherent age population of the data set (316 ± 2 Ma). Compared to the predominant 273 Ma monazite age population and monazite from samples AS07 and AS06, this age population is characterized by higher Y concentrations (mean value of 2,048 ppm, n = 6), lower values of Th/U (mean Th/U value of 6; Figure S12), and higher X_I scores. These observations support the interpretation that the 316 Ma age population records the timing of prograde metamorphism prior to significant garnet growth. Further support is drawn from the presence of rutile inclusions within monazite VII (AS13); petrographic, phase equilibria, and trace-element observations from numerous other IVZ metapelites show that rutile formed during the prograde breakdown of high-Ti biotite and concomitant melt production (Luvizotto & Zack, 2009).

9. Correlation of Garnet and Monazite Domains

To further constrain the PT evolution of IVZ metapelites, we used monazite-garnet HREE partitioning to determine which garnet and monazite domains coexisted (e.g., Buick et al., 2006; Hacker et al., 2019; Hermann & Rubatto, 2003; Jiao et al., 2021; Mottram et al., 2014; Pyle et al., 2001; Rubatto et al., 2006; Warren et al., 2019). Given the expected temperature dependence of this partitioning (e.g., Hacker et al., 2019) and the absence of experimentally derived monazite-garnet partition coefficients (D), we used the empirically derived partition coefficients from Hermann and Rubatto (2003) to identify monazite and garnet zones that record chemical equilibrium. This approach is advantageous because these D values were derived from a Variscan lower crustal metapelite from Val Malenco, Northern Italy, that experienced notably similar metamorphic conditions to granulite-facies samples of the IVZ (~10 kbar and 650–750°C). For each sample we calculate $D_{Gd\text{-}Lu}$ using the average monazite composition of each of the age populations identified in Section 8 in combination with all garnet analyses; arrays of $D_{Gd\text{-}Lu}$ are then compared to $D_{Gd\text{-}Lu}$ from Hermann and Rubatto (2003). A summary of these comparisons is displayed in Figure 9, while a complete set of monazite-garnet $D_{Gd\text{-}Lu}$ arrays is presented in Figure S13.

Values of $D_{Gd\text{-}Lu}$ calculated for monazite from the 290 Ma age population of sample MW19 are in good agreement with those from Hermann and Rubatto (2003) for all garnet compositions, excluding three of the outermost

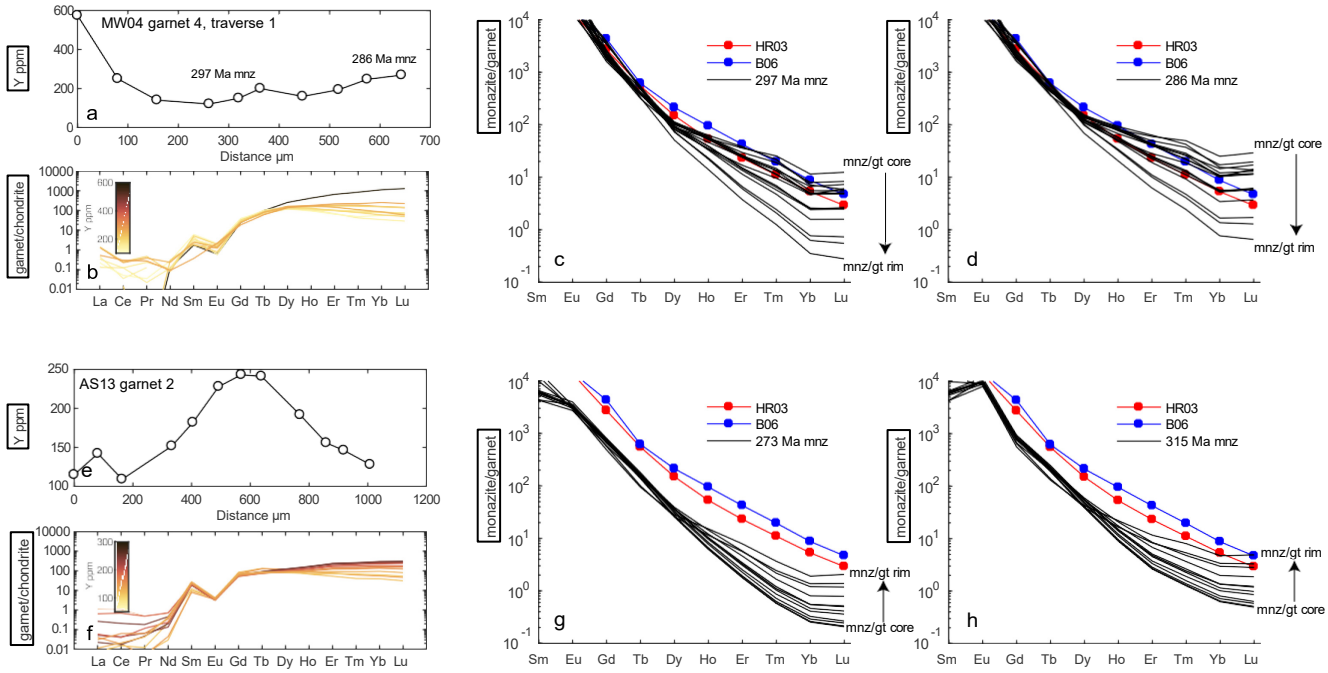

Figure 9. Garnet trace element compositions and garnet-monazite partitioning. Panels show Y concentrations (a, e) and chondrite-normalized REE patterns shaded for Y concentration (b, f) along rim-to-rim transects across garnet 4, MW04 and garnet 2, AS13, respectively. Panels c and d and g–h show arrays of $D_{Sm\text{-}Lu}$ calculated for various monazite age populations and the garnet compositional profiles shown in A and E, respectively. Red and blue markers correspond to partitioning arrays from Hermann and Rubatto (2003) and Buick et al. (2006), respectively.

garnet rim compositions. This implies that garnet growth occurred in this sample around 290 Ma; in contrast, monazite from the older, 296 Ma age population yield values of $D_{Dy\text{-}Lu}$ that are systematically lower than those from Hermann and Rubatto (2003), consistent with monazite core equilibration prior to the onset of garnet core growth. The absence of a garnet population that coexisted with HREE-fractionated monazite core domains implies that either such garnet was resorbed during cooling prior to growth of the monazite rim domains at ~290 Ma, or that the temperatures of monazite core-garnet equilibration were significantly different to those from which the Hermann and Rubatto (2003) D values are derived.

For sample MW04, the observed rimward increase in garnet Y + HREE concentrations corresponds to best-fit $D_{Gd\text{-}Lu}$ between garnet core compositions and the 297 Ma monazite age population, whereas garnet rims appear to have equilibrated with the 286 Ma monazite age population (Figures 9a–9d). The smooth increase in Y + HREE concentrations toward garnet rims can be explained either by diffusive equilibration of garnet rims during resorption or by protracted garnet growth during dissolution of a Y + HREE-enriched mineral phase. Regarding the former, we note that the observed Y zonation length scale of ~200 µm (Figure 9a) implies unrealistically long timescales for diffusive equilibration at the peak temperatures derived from phase equilibria (~65 Myr at ~800°C, Figure 5; calculations use Arrhenian diffusivity parameters reported by Bloch et al., 2020); temperatures >870°C are required for such diffusion to occur over 10 Myr. Accordingly, we prefer the interpretation that garnet growth is bracketed by the timing of monazite core and rim equilibration, between 297 and 286 Ma, respectively.

Monazite from the 277 Ma age population from sample MW03 yields similar $D_{Gd\text{-}Lu}$ to the values reported by Hermann and Rubatto (2003) for all garnet compositions (Figure S13), reflecting the absence of pronounced core-to-rim Y + HREE zonation in garnet from this sample (Figure S7). Values of $D_{Dy\text{-}Lu}$ calculated using the 292 Ma monazite population are systematically offset toward lower values. We interpret that the observed garnet population equilibrated with monazite rims around 277 Ma. Similar to the preferred interpretation for sample MW19, the absence of a garnet population in equilibrium with monazite cores requires that either such garnet was resorbed during cooling prior to 277 Ma, or such garnet growth occurred under significantly different PT conditions.

Figures 9e–9g shows that the well-defined bell-shaped Y + HREE garnet profiles for granulite-facies sample AS13 have sufficiently elevated concentrations to produce monazite-garnet partition coefficients, $D_{Gd\text{-}Lu}$, that are lower than Hermann and Rubatto's by up to half an order of magnitude. We note that the shape of the $D_{Er\text{-}Lu}$ portion of the partition coefficient array is flatter than observed in the amphibolite-facies samples. The disagreement between expected and observed monazite-garnet partitioning implies that both the 316 Ma and 273 Ma monazite age populations did not equilibrate with the observed garnet population and that, presumably, garnet growth occurred at some time between the timing of the two monazite age peaks. This conclusion is further supported for the older monazite population by the presence of included monazite in garnet. However, garnet in amphibolite- and granulite-facies metapelites often shows evidence of pervasive recrystallization of pre-existing core domains during near-peak metamorphic conditions (e.g., Yardley & Barber, 1991), so these data may also suggest that the garnet in equilibrium with 316 Ma monazite is no longer extant in sample AS13.

10. Discussion

10.1. Constraints on the Timing of Regional Prograde and High-Temperature Metamorphism

The best quantitative constraint on the timing of regional metamorphism in the IVZ that predated emplacement of the Mafic Complez (e.g., Barboza et al., 1999) comes from the oldest monazite age population preserved in sample AS13 (316 ± 2 Ma, MSWD = 0.8, n = 6). This age population corresponds to monazite included in garnet and with lower X_1 scores than the amphibolite-facies samples. Despite the absence of monazite-garnet HREE equilibrium for this age population, the composition of such monazite implies that prograde or peak garnet growth and, by inference, regional metamorphism in the central sector of the IVZ initiated before ~316 Ma. This is remarkably similar to existing zircon-based constraints on the timing of regional high-temperature metamorphism in the Val Strona section, which we discuss further in the next paragraph.

Ewing et al. (2013) interpreted a 316 ± 3 Ma population of U-Pb zircon analyses with Ti-in-zircon temperatures between 750°C and 800°C as recording cooling from the climax of amphibolite-to-granulite-facies regional metamorphism. These data were acquired from a sample (IVT-20) collected at the base of Val Strona di Omegna, <1.5 km structural distance from the locality of sample AS13 (*this study*). A similar 315 Ma U-Pb zircon intrusion date was obtained by Klötzli et al. (2014) on a garnet-bearing metagabbro (Monte Capio sill) at the base of the Val Strona section, indicating mafic magmatism had initiated by that time. Kunz et al. (2018) reported similar zircon U-Pb dates of 316 ± 16 Ma (IZ 407) and 312 ± 22 Ma (IZ 412) from Val Strona and Val Sesia metapelites, respectively, but noted that the 316 ± 3 Ma population observed by Ewing et al. (2013) was uncommon in the IVZ. Guergouz et al. (2018) obtained U-Pb dates as old as 334 ± 5 Ma from amphibolite-facies zircon rims (sample IZ-129), but did not ascribe geological significance to individual analyses, instead using the interquartile range of pooled zircon data to propose that peak amphibolite-facies conditions were attained by 310 Ma. We note that the same study also reported a monazite U-Pb date of 323 ± 8 Ma (sample IZ-134) from a xenomorphic monazite hosted in garnet.

Because the oldest mafic magmatic dates in Val Strona are ~314 Ma (Klötzli et al., 2014), but IVZ mafic magmatism was volumetrically insignificant until ~286 Ma (Karakas et al., 2019), heating by mafic sill emplacement is insufficient to explain the elevated metamorphic temperatures suggested by oldest, pre-315 Ma prograde monazite dates preserved in both amphibolite- and granulite-facies samples. Other viable heating mechanisms are underthrusting of the sediments in an accretionary wedge (e.g., Handy et al., 1999), or elevated conductive heat flow through a thinned mantle lithosphere (e.g., Henk et al., 1997).

Though most of the petrologic (Kunz & White, 2019; Redler et al., 2012) and geochronologic record of the IVZ shows that the extant metamorphic assemblages record peak to post-peak metamorphic conditions (as argued here), there is evidence for an early phase of metamorphism that was characterized by higher-P, lower-T conditions, prior to the attainment of peak temperatures. This is manifest as: (a) relict kyanite overgrown by sillimanite in IVZ metapelites (Bertolani, 1959; Boriani, 1971; Capedri, 1971; Handy, 1987); (b) relict staurolite enclosed by cordierite (Zingg, 1980), and (c) the presence of retrogressed eclogites and kelyphitic peridotites in the uppermost levels of the IVZ (Boriani & Peyronel Pagliani, 1968; Handy et al., 1999; Lensch, 1972). Although not unequivocal, these lines of evidence are consistent with the interpretation that IVZ lithologies underwent contractional deformation and prograde metamorphism in a Varsican accretionary wedge (Handy et al., 1999), as proposed for the overlying Strona-Cenari Zone (Boriani & Villa, 1997). Detrital zircon cores from IVZ metasediments yield a

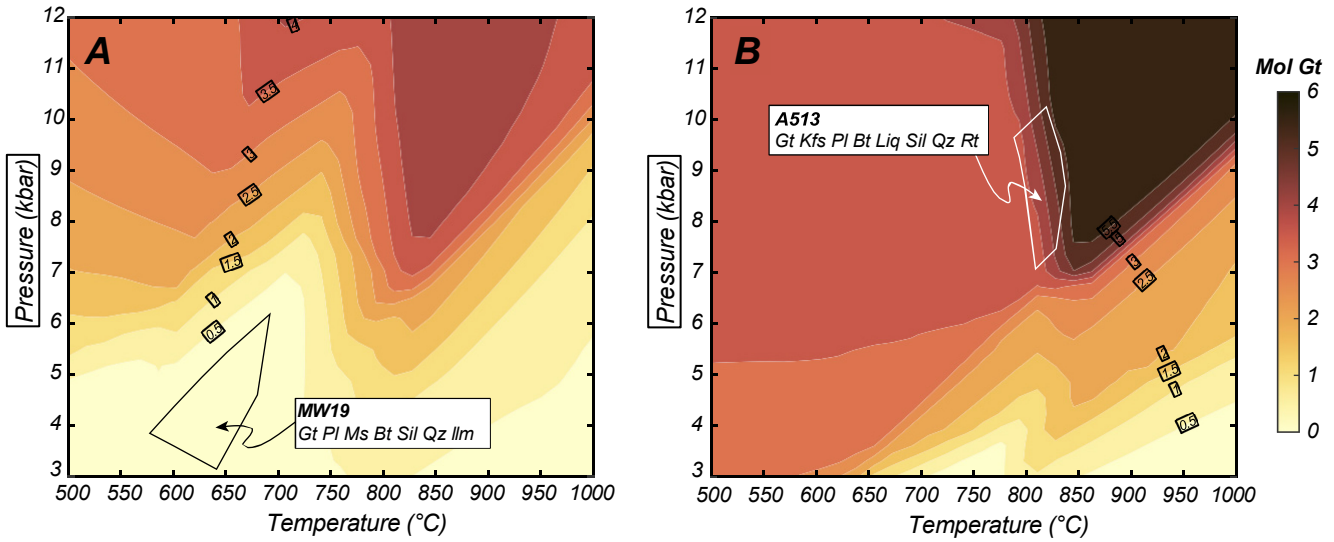

Figure 10. Calculated *PT* isomodes of garnet abundance (mols) for sample MW19 and AS13. Outlines correspond to peak metamorphic conditions for each sample.

population of U-Pb dates that constrains the maximum depositional age of the sedimentary package to ~350 Ma (Kunz et al., 2018; Vavra & Schaltegger, 1999). Combined with our monazite Th-Pb dates and garnet-present compositions, this provides a restricted time interval of <30 Myr for zircon production (i.e., arc volcanism), sedimentation, burial and heating to peak temperatures.

10.2. High-Temperature Decompression

The curvilinear increase in X_I scores exhibited by monazite from six of the eight amphibolite-facies samples suggests increases and decreases of the influence of plagioclase and garnet, respectively, on monazite composition from ~310 to ~280 Ma (Figure 8). It is noteworthy that the initiation of this trend systematically occurs at younger ages with increasing depth, from ~310 Ma for sample MW23, to ~290 Ma for sample MW04. To link this trend in monazite chemistry to *PT* evolution, Figure 10 shows contours of garnet mode calculated for samples MW19 and AS13. Relative to peak metamorphic conditions (Figure 5), calculated garnet modes decrease at the expense of plagioclase with decreases in pressure and either increases or decreases in temperature. Therefore, we interpret the X_I trend exhibited by amphibolite-facies monazite as representing decompression following the peak of regional metamorphism. Notably, this exhumation initiated 4–24 Myr prior to emplacement of the Mafic Complex and the dominant phase of mafic magmatism in the IVZ at 286-282 Ma (Karakas et al., 2019), with the locus of monazite growth propagating downsection with time through the amphibolite-facies portion of the IVZ. This age pattern may record the crossing of a specific "monazite-in" isotherm that occurred at a relatively constant temperature throughout IVZ section (see also Section 10.3). An implication of the inferred monazite exhumation signal is that the interpreted "peak" mineral parageneses have actually been frozen in during exhumation and that the *PT* conditions derived from these assemblages may not accurately reflect peak *P* or *T* conditions, as is traditionally interpreted (e.g., Redler et al., 2012). For example, the lower amphibolite-facies sample MW23 does not currently contain garnet, yet monazite with dates >300 Ma is characterized by steep MREE-HREE patterns (X_I scores <2), consistent with growth in the presence of garnet.

Interestingly, the monazite-garnet HREE partitioning constraints on the timing of garnet growth (Section 9) imply that amphibolite-facies (and potentially granulite-facies) garnets grew or chemically re-equilibrated >20 Myr after the inferred peak of regional metamorphism at ~316 Ma, during decompression (mnz/gt timing of garnet equilibration for MW19: 290 Ma; MW04: 297–286 Ma; MW03: 277 Ma). This is intriguing because the compositions of the oldest monazite populations in granulite-facies sample AS13 (X_I < −2 at 316 ± 2 Ma) imply coexistence with at least some garnet; this assertion is strengthened by the fact that the inferred regional peak metamorphic temperatures at ~316 Ma (750°C–800°C, Ewing et al., 2013) would have produced abundant garnet in such fertile metapelitic bulk compositions. A possible explanation for the disappearance of widespread garnet related to pre-300 Ma metamorphism is consumption or recrystallization of garnet during cooling and/or decompression

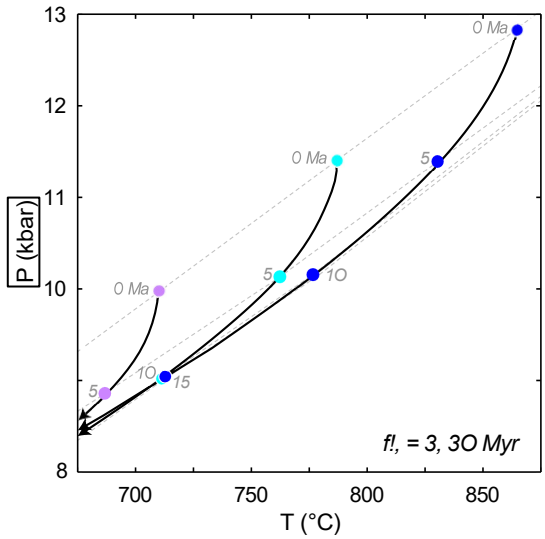

Figure 11. *PT* paths for extending continental crust. Plot shows *PT* trajectories for three rocks, initially located at 30 (purple), 35 (cyan) and 40 km (blue) depth. Dashed lines are geotherms at 0, 5, 10 and 15 Ma. The calculations were performed following the scheme presented by Smye et al. (2019) and assume a crustal thinning factor of 3 over 30 Myr, and an initial lithospheric thickness of 100 km of which the upper 50 km is treated as continental crust.

from peak temperatures. This interpretation is supported by the steep Clapeyron slopes of garnet isomodes for both amphibolite- and granulite-facies metapelitic compositions at 700°C–850°C and 6–12 kbar (Figure 10). While quantitative determination of *PT* paths awaits further investigation, we note that a similar evolution of garnet growth was determined for the Val Malenco metapelitic granulites (Hermann & Rubatto, 2003).

It is noteworthy that monazite from the granulite-facies samples does not preserve a record of the inferred decompression (Figure 8). Primarily, this can be explained by the gap in monazite dates between ~300 and ~285 Ma in samples AS13 and AS07. However, monazite with dates <290 Ma in the granulite-facies samples is characterized by lower X_I values than amphibolite-facies monazite—independent of Th-Pb date—implying a stronger influence of garnet on monazite composition throughout IVZ metamorphism than in the overlying amphibolite-facies metasediments. A plausible explanation for this buffering of monazite composition is that temperatures at the base of the lower crustal section remained sufficiently elevated after decompression to preserve abundant garnet, and thus emplacement of the Mafic Complex only led to minor garnet resorption in the deepest and highest-grade samples (e.g., Figure 12). This corroborates the interpretation of Ti-in-zircon temperatures of Ewing et al. (2013) that ambient temperatures at the base of the IVZ were >740°C–800°C until ~260 Ma.

Figure 11 shows the *PT* paths predicted for three rocks, initially located at depths of 30, 35 and 40 km in an extending crustal column (see figure caption for specific calculation parameters). Although the form of each of the *PT* paths is similar and reflects cooling during extensional decompression, the duration to attain a specific *PT* condition increases with depth. For example, <700°C conditions are attained in <5 Myr for the shallowest rock (purple marker), ~12 Myr for the intermediate depth sample (cyan) and ~16 Myr for the deepest sample (blue). If the decompression trend reflects monazite growth over a discrete *PT* interval where garnet isomodes are tightly spaced—and that *PT* interval is similar among samples—it would seem reasonable to interpret the downward younging signal as representing the progressive exhumation of the deep crust in an extensional strain field. An alternative explanation requires stratification of extensional strain such that deformation across the amphibolite-facies depth interval was decoupled from the underlying granulite-facies rocks. Such decoupling of the upper and lower crust during extension would be expected should the lowermost crust behave as a viscous channel, as assumed in models of lower crustal flow (e.g., Hopper & Buck, 1996; McKenzie et al., 2000).

Decompression of the amphibolite-facies portion of the Val Strona IVZ section subsequent to the attainment of peak metamorphic temperatures also explains several independent petrological and structural observations: (a) overprinting of the regional high-temperature metamorphic assemblage by a lower-pressure cordierite-bearing assemblage in rocks adjacent to the Mafic Complex in Val Sesia and Val Strona di Postua (Barboza & Bergantz, 2000; Redler et al., 2012); (b) the presence of retrograde muscovite and the absence of cordierite in metapelites outside of the Mafic Complex aureole (Barboza & Bergantz, 2000); (c) the presence of orthopyroxene + plagioclase + spinel symplectites, presumably after garnet, in metapelite from the deepest section of Val Strona di Omegna (Brodie, 1995); (d) the presence of high-temperature mylonitic shear zones in the upper amphibolite- and granulite-facies sections of the IVZ (Brodie & Rutter, 1987) that accommodated extensional deformation prior to 280 Ma (Brodie et al., 1989; Brodie & Rutter, 1987); (e) the arcuate magmatic foliation preserved in the uppermost Mafic Complex, interpreted by Quick et al. (1994) to represent emplacement into a zone of active extension, and (f) non-coaxial, ductile deformation within metasediments adjacent to the Mafic Complex (Snoke et al., 1999). A similar high-*T* event, characterized by ~2 kbar of decompression, marked the termination of Variscan granulite-facies metamorphism in the Calabrian lower crustal terrane that is considered analogous to the IVZ (Schenk, 1990).

The most precise constraint on the magnitude of IVZ decompression was made by Redler et al. (2012), who demonstrated that metasediments adjacent to the Mafic Complex in Val Sesia yield peak metamorphic conditions

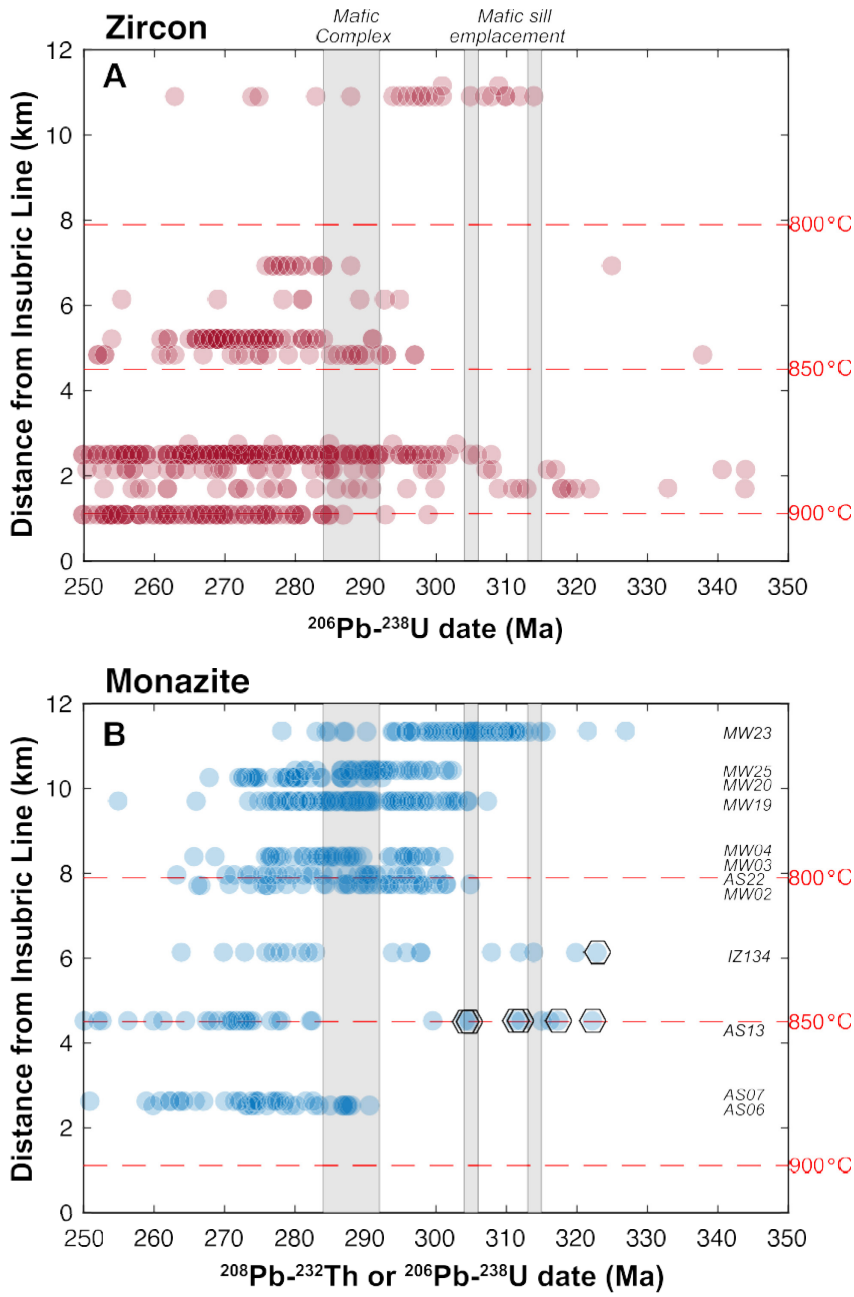

Figure 12. Comparison between zircon U-Pb and monazite U/Th-Pb spot dates along Val Strona di Omegna. Zircon dates are plotted from Vavra and Schaltegger (1999), Ewing et al. (2013), Guergouz et al. (2018), Kunz et al. (2018). Monazite data are from *this study* and sample IZ134 from Guergouz et al. (2018). Dashed lines correspond to the structural position of isotherms inferred from the field gradient reported by Redler et al. (2012). Hexagonal markers denote analyses from monazite grains included within garnet.

of more than 800°C at pressures of ~6 kbar, significantly lower pressures than the equivalent temperatures along the Val Strona transect (6–9 kbar at 750°C–800°C). Their estimate of ~1–2 kbar of decompression is consistent with the minimum magnitudes of decompression estimated by Barboza and Bergantz (2000).

10.3. Comparison With Zircon U-Pb Dates

Figure 12 shows a comparison between published zircon U-Pb spot dates from metasediments along Val Strona di Omegna with monazite Th-Pb dates presented in this study. Spot dates for each sample are plotted against

distance from the Insubric Line and overlaid on inferred peak temperatures from the *PT* gradient reported by Redler et al. (2012); in this reference frame, inferred peak *P* increases closer to the Insubric Line. Inspection of the figure reveals a broad decrease in zircon and monazite spot dates with increasing structural depth, although the trend is more consistent in the monazite data; the majority of zircon and monazite spot dates from amphibolite-facies samples (peak-*T* <800°C) are older than the dominant magmatic phase of the Mafic Complex (282–286 Ma; Karakas et al., 2019). Despite localized mafic sill emplacement (Figure 12; Monte Capio Sill, Albo Sill, Klötzli et al., 2014), the preservation of dates >300 Ma implies that the thermal effects of Permian magmatism in the amphibolite-facies section of the Val Strona section were insufficient to facilitate widespread dissolution of monazite or zircon.

A key difference between the zircon and monazite datasets is the preservation of prograde metamorphic and inherited zircon cores (analyses with U-Pb dates >330 Ma) in samples that experienced peak conditions greater than ~800°C. Monazite Th-Pb dates >310 Ma in these granulite-facies samples are preserved predominantly in grains included within garnet (black outlines on Figure 12b); the vast majority of monazite analyses from granulite-facies samples post-date, or are contemporaneous with, emplacement of the Mafic Complex, ~30 Myr younger than the inferred age of the thermal climax (~316 Ma, Ewing et al., 2013). These observations imply that prograde and inherited monazite was efficiently resorbed in samples that experienced peak temperatures >800°C during the regional Permo-Carboniferous high-temperature metamorphic event that preceded voluminous mafic magmatism. This is corroborated by the neoblastic morphologies of monazite in upper amphibolite- and granulite-facies samples along Val Strona di Omegna (Figures 3 and 4; Bea & Montero, 1999) and both experimental (Stepanov et al., 2012) and theoretical constraints (Kelsey et al., 2008; Yakymchuk & Brown, 2014) on the solubility of monazite in felsic melts. In contrast, dissolution of zircon in samples of comparable grade was partial (e.g., Kunz et al., 2018).

While there are numerous inherited zircon U-Pb dates, the majority of monazite and zircon U-Th-Pb dates post-date the regional thermal climax at ~316 Ma, and indeed most granulite-facies zircon and monazite grew after the intrusion of the Mafic Complex from ~286 to 282 Ma. One explanation for the absence of old dates, as well as the pattern of downsection younging monazite and zircon U-Pb dates, is protracted residence of the middle-to-lower crustal IVZ at temperatures above those required for zircon and monazite saturation. Klötzli et al. (2014) proposed such an interpretation to account for an apparent gap in zircon dates from 316 ± 3 Ma to 276 ± 4 Ma, observed in the deep-crustal granulite-facies paragneiss of the IVZ that overlaps a gap from circa 314 to 283 Ma between igneous and reset zircons in a closely associated mafic–ultramafic sill. Subsequently measured zircon U-Pb dates (e.g.,Kunz et al. (2018)) reveals continuous (re)crystallization of zircon after ~305 Ma in metasediments along along Val Strona di Omegna. In contrast, Ewing et al. (2013) argued for significant cooling following peak metamorphic conditions at ~316 Ma, prior to renewed heating associated with emplacement of the Mafic Complex at 282–286 Ma (Karakas et al., 2019). We note that the timing of this cooling is consistent with it being related to the decompression that occurred prior to and during emplacement of the Mafic Complex. Because decompression and cooling from peak temperatures is predicted to cause crystallization of zircon- and monazite-saturated melts resident in the deep crust (e.g., Yakymchuk & Brown, 2014), we interpret the distribution of monazite and zircon U-Th-Pb dates along Val Strona di Omegna to reflect high-temperature cooling on extensional decompression of the Variscan root zone. The age patterns displayed by monazite and zircon reflect the crossing of each portion of the IVZ through a specific interval of monazite and zircon saturation during this cooling episode, and are consistent with timescales of cooling from peak *T* varying from ~25 Myr at the top of the section to ~100 Myr at the base. Implicit to this interpretation is that the thermal effects of emplacement of Mafic Complex were short-lived (e.g., Peressini et al., 2007) and spatially restricted (e.g., Barboza & Bergantz, 2000).

11. Implications for the Assembly and Tectonic Evolution of Continental Lower Crust

Our data constrain the onset of prograde metamorphism in IVZ metasediments to ~316 Ma Ma. Combined with the youngest reported detrital zircon dates of ~350 Ma from IVZ metasediments, this implies that clastic sediment deposition, burial to 7–10 kbar and prograde heating to amphibolite-to-granulite-facies temperatures occurred over a timespan of <30 Ma (see Figure 13 for a tectonic summary). This assembly timescale for the IVZ metasediments cannot be ascribed to differences in structural position because sample AS13—host to the oldest monazite age population in our dataset—was collected from within ~200 m of a sample that yields zircon with detrital core U-Pb dates of 352 ± 16 Ma (sample IZ407, Kunz et al., 2018). Such short metamorphic

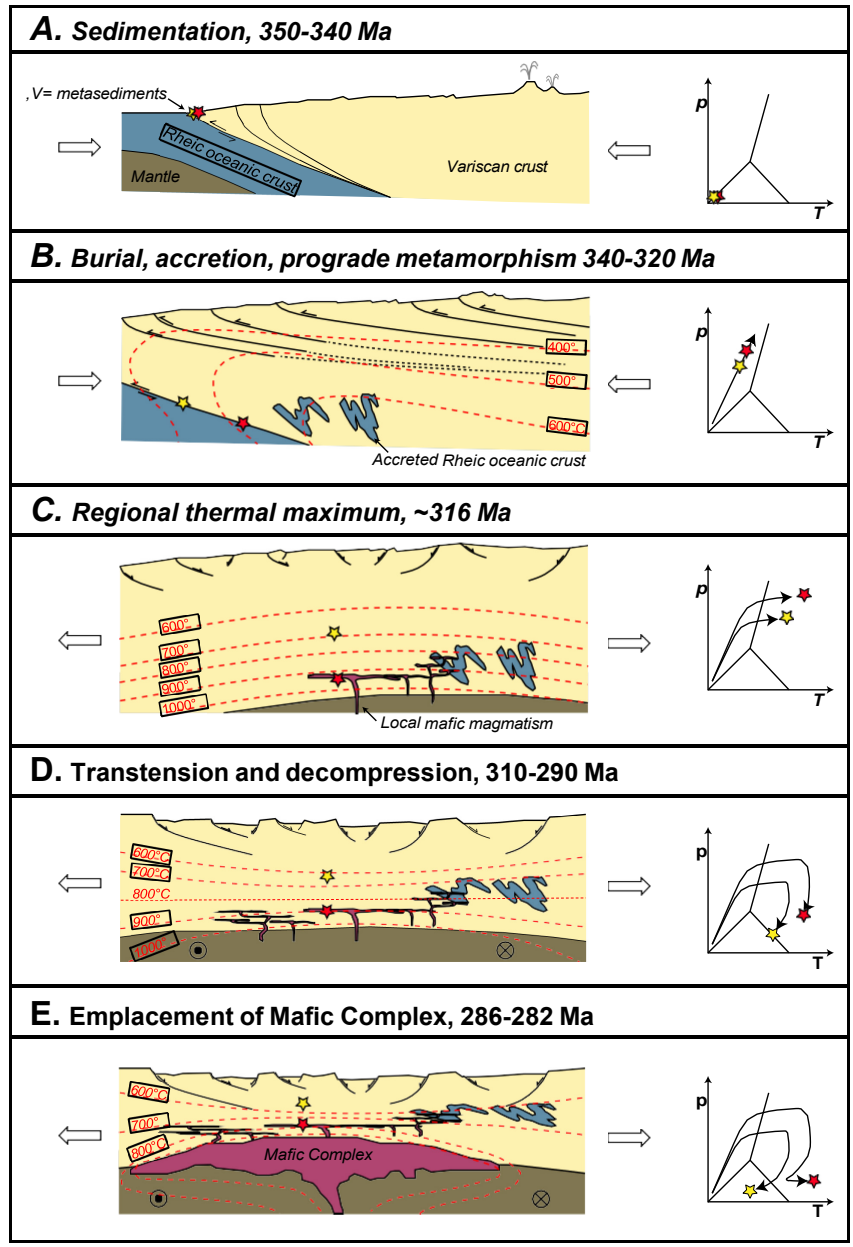

Figure 13. Inferred tectonic evolution of Ivrea-Verbano Zone (IVZ) metasediments. Isotherms and pressure-temperature (*PT*) paths are schematic and intended to show the evolution of the crustal thermal gradient. Yellow and red stars represent metasediments in the upper and lower structural domains of the Val Strona transect, respectively. Sedimentation of the IVZ metasediments in a Variscan accretionary wedge (a) was followed by burial, imbrication and prograde metamorphism within the kyanite stability field (b). Minor mafic magmatism accompanied heating of the accreted sediments and attainment of the regional Variscan thermal climax within the sillimanite stability field (c). The onset of transtensional decompression resulted in cooling and exhumation (d) prior to emplacement of the Mafic Complex and contact metamorphism within the andalusite stability field (e).

timescales demand elevated thermal gradients, in excess of those predicted to occur in orogenically thickened crust (England & Thompson, 1984). A potential mechanism that accounts for such rapid metamorphic timescales is the accretion of sediments during underthrusting beneath a continental magmatic arc system. First proposed for the IVZ by Sills and Tarney (1984), this tectonic interpretation accounts for the diversity of sedimentary and mafic pre-Permian lithologies and a prograde evolution within the kyanite *PT* stability field (Handy et al., 1999). Similar, if not shorter, timescales for the deposition, underthrusting, accretion and metamorphism of lower

crustal metasediments have been reported in other arc settings—e.g., the Cascades (Matzel et al., 2004; Sauer et al., 2018) and the Coast Ranges of California (Ducea et al., 2009; Grove et al., 2003).

Accretion of the IVZ metasediments was rapidly followed by the onset of decompression and extensional deformation. In the shallowest samples, decompression-related cooling initiated as early as ~310 Ma, a minimum of ~5 Myr after peak temperatures, and implying that much of the high-temperature history of the IVZ (including most preserved metamorphic assemblages and textures) occurred within an extensional tectonic regime. Convective removal of a lithospheric root beneath thickened Variscan lithosphere is one plausible explanation for this tectonic switch (e.g., Handy et al., 1999; Ménard & Molnar, 1988; Zingg et al., 1990). Platt and England (1994) showed that foundering of dense mantle lithosphere is expected to drive asthenospheric upwelling, mantle melting and regional lithospheric extension immediately following root removal; conductive heating of the deep crust is governed by the time constant of the overlying lithosphere. We note that this explanation accounts for the persistence of high-temperature conditions during decompression observed in the IVZ as well as the emplacement of mantle-derived melts. A similar tectonic evolution has been proposed for metasedimentary lower crust of the southern Rio Grande Rift, which is actively experiencing granulite-facies metamorphism at comparable *PT* conditions to those preserved in metapelites at the base of Val Strona di Omegna (e.g., Cipar et al., 2020).

12. Conclusions

1. Monazite Th-Pb dates from amphibolite-to-granulite-facies metapelites exposed along the Val Strona di Omegna transect of the IVZ preserve a protracted record of Permo-Carboniferous metamorphism, spanning >320 Ma to <250 Ma. Intrasample monazite Th-Pb date ranges decrease with increasing metamorphic grade and structural depth
2. Variance in monazite TE compositions is dominated by the effects of plagioclase and garnet partitioning on Sr, Y, MREE and HREE concentrations
3. Monazite growth occurred under prograde or peak amphibolite-to-granulite-facies conditions by 316 ± 2 Ma. Combined with existing detrital zircon U-Pb dates from Val Strona di Omegna, the monazite data define a <30 Myr duration for the deposition of clastic sediments and their burial and heating to >700°C
4. Amphibolite-facies monazite defines a temporal trend in TE composition that is consistent with a progressive decrease in the modal abundance of garnet after ~310 Ma. The *PT* distribution of garnet modes in amphibolite-facies metapelites implies that this trend was caused by decompression following peak metamorphic conditions. The timing of the onset of decompression-related cooling decreases to ~290 Ma at the base of the amphibolite-facies portion of the crustal section
5. Granulite-facies monazite equilibrated under garnet-present *PT* conditions between ≥290 and <250 Ma
6. Similar short timescales for the deposition, burial and prograde metamorphism of lower crustal sediments have been reported from other continental magmatic arc terranes. This lends support to the interpretation that the pre-Permian lithologies in the IVZ were accreted to the base of a Variscan magmatic arc system >10 Myr prior to the onset of regional extension and mafic magmatism

Data Availability Statement

All data supporting the conclusions in this paper are contained in Tables 1 and 2 and supporting information Tables S1–S3. These data are freely available online at this site: https://doi.org/10.17605/OSF.IO/QHJ45.

Acknowledgments
This research was funded by Penn State and NSF grant 1927631 to AJS and 1927635 to BH. AJS acknowledges support from the Slingerland Early Career Professorship. Andrew Kylander-Clark is thanked for assistance with the LASS analyses at UCSB. Dr Stan Mertzman performed XRF analyses at Franklin and Marshall. JMG acknowledges support from NSF Grant OISE-1545903. Critical reviews by Jörg Hermann, Urs Klötzli and two anonymous reviewers served to improve the manuscript; we are also grateful for Laurent Jolivet's deft editorial handling.

References

Aitchison, J. (1983). Principal component analysis of compositional data. *Biometrika*, *70*(1), 57–65.
Aleinikoff, J. N., Schenck, W. S., Plank, M. O., Srogi, L., Fanning, C. M., Kamo, S. L., & Bosbyshell, H. (2006). Deciphering igneous and metamorphic events in high-grade rocks of the Wilmington Complex, Delaware: Morphology, cathodoluminescence and backscattered electron zoning, and SHRIMP U-Pb geochronology of zircon and monazite. *The Geological Society of America Bulletin*, *118*(1–2), 39–64.
Babist, J., Handy, M., Konrad-Schmolke, M., & Hammerschmidt, K. (2006). Precollisional, multistage exhumation of subducted continental crust: The Sesia Zone, Western Alps. *Tectonics*, *25*(6).
Barboza, S. A., & Bergantz, G. W. (2000). Metamorphism and anatexis in the mafic complex contact aureole, Ivrea Zone, Northern Italy. *Journal of Petrology*, *41*(8), 1307–1327.
Barboza, S. A., Bergantz, G. W., & Brown, M. (1999). Regional granulite facies metamorphism in the Ivrea zone: Is the Mafic Complex the smoking gun or a red herring? *Geology*, *27*(5), 447–450.

Bea, F., & Montero, P. (1999). Behavior of accessory phases and redistribution of Zr, REE, Y, Th, and U during metamorphism and partial melting of metapelites in the lower crust: An example from the Kinzigite Formation of Ivrea-Verbano, NW Italy. *Geochimica et Cosmochimica Acta*, *63*(7–8), 1133–1153.

Behn, M. D., & Kelemen, P. B. (2003). Relationship between seismic P-wave velocity and the composition of anhydrous igneous and meta-igneous rocks. *Geochemistry, Geophysics, Geosystems*, *4*(5).

Bertolani, M. (1959). La formazione basica "Ivrea-Verbano" e la sua posizione nel quadro geologico-petrografico della Bassa Val Sesia e del Biellese. *Periodico di Mineralogia*, *28*, 151–209.

Bloch, E. M., Jollands, M. C., Devoir, A., Bouvier, A. S., Ibañez-Mejia, M., & Baumgartner, L. P. (2020). Multispecies diffusion of yttrium, rare earth elements and hafnium in garnet. *Journal of Petrology*, *61*(7), egaa055.

Boriani, A. (1971). Geology of the junction between the Ivrea-Verbano and Strona-Ceneri zones (Southern Alps).

Boriani, A., Caironi, V., & Sacchi, R. (2016). The CMB line: The southern margin of the Ivrea–Verbano zone (basement of Southern Alps, Italy): A re-appraisal. *Rendiconti Lincei*, *27*(4), 673–678.

Boriani, A., & Giobbi, E. (2004). Does the basement of western southern Alps display a tilted section through the continental crust? A review and discussion. *Periodico di Mineralogia*, *73*(2), 5–22.

Boriani, A., Origoni, E. G., Borghi, A., & Caironi, V. (1990). The evolution of the "Serie dei Laghi"(Strona-Ceneri and Scisti dei Laghi): The upper component of the Ivrea-Verbano crustal section; Southern Alps, north Italy and Ticino, Switzerland. *Tectonophysics*, *182*(1–2), 103–118.

Boriani, A., & Peyronel Pagliani, G. (1968). Rapporti fra le plutoniti erciniche e le metamorfiti del Massiccio dei Laghi nella zona del M. Cerano (Bassa Val d'Ossola). *Rendiconti della Societa Italiana di Mineralogia e Petrologia*, *24*, 111–142.

Boriani, A., & Villa, I. M. (1997). Geochronology of regional metamorphism in the Ivrea-Verbano zone and Serie dei Laghi, Italian Alps. *Schweizerische Mineralogische und Petrographische Mitteilungen*, *77*, 381–401.

Brack, P., Ulmer, P., & Schmid, S. M. (2010). A crustal-scale magmatic system from the Earth's mantle to the Permian surface: Field trip to the area of lower Valsesia and Val d'Ossola (Massiccio dei Laghi, Southern Alps, Northern Italy). *Swiss Bulletin für angewandte Geologie*, *15*(2), 3–21.

Brodie, K. (1995). The development of orientated symplectites during deformation. *Journal of Metamorphic Geology*, *13*(4), 499–508.

Brodie, K., & Rutter, E. (1987). Deep crustal extensional faulting in the Ivrea Zone of northern Italy. *Tectonophysics*, *140*(2–4), 193–212.

Brodie, K., Rutter, E., & Evans, P. (1992). On the structure of the Ivrea-Verbano Zone (northern Italy) and its implications for present-day lower continental crust geometry. *Terra Nova*, *4*(1), 34–40.

Brodie, K., Rutter, E., & Rex, D. (1989). On the age of deep crustal extensional faulting in the Ivrea zone, northern Italy. *Geological Society, London, Special Publications*, *45*(1), 203–210.

Brown, E. H., & Walker, N. W. (1993). A magma-loading model for Barrovian metamorphism in the southeast Coast Plutonic complex, British Columbia and Washington. *The Geological Society of America Bulletin*, *105*(4), 479–500.

Buick, I. S., Hermann, J., Williams, I. S., Gibson, R. L., & Rubatto, D. (2006). A SHRIMP U–Pb and LA-ICP-MS trace element study of the petrogenesis of garnet–cordierite–orthoamphibole gneisses from the Central Zone of the Limpopo Belt, South Africa. *Lithos*, *88*(1–4), 150–172.

Burke, M. M., & Fountain, D. M. (1990). Seismic properties of rocks from an exposure of extended continental crust—New laboratory measurements from the Ivrea Zone. *Tectonophysics*, *182*(1–2), 119–146.

Capedri, S. (1971). Sulle rocce della formazione basica Ivrea-Verbano. II. Petrografia delle granuliti e rocce derivate affioranti nella Val Mastallone (Vercelli) e loro evoluzione petrogenetica. *Memorie della Società geologica italiana*, *10*, 227–312.

Carvalho, B. B., Bartoli, O., Ferri, F., Cesare, B., Ferrero, S., Remusat, L., et al. (2019). Anatexis and fluid regime of the deep continental crust: New clues from melt and fluid inclusions in metapelitic migmatites from Ivrea Zone (NW Italy). *Journal of Metamorphic Geology*, *37*(7), 951–975.

Cipar, J. H., Garber, J. M., Kylander-Clark, A. R., & Smye, A. J. (2020). Active crustal differentiation beneath the Rio Grande Rift. *Nature Geoscience*, *13*(11), 758–763.

Coggon, R., & Holland, T. (2002). Mixing properties of phengitic micas and revised garnet-phengite thermobarometers. *Journal of Metamorphic Geology*, *20*(7), 683–696.

Condie, K. C. (1999). Mafic crustal xenoliths and the origin of the lower continental crust. *Lithos*, *46*(1), 95–101.

De Capitani, C., & Brown, T. H. (1987). The computation of chemical equilibrium in complex systems containing non-ideal solutions. *Geochimica et Cosmochimica Acta*, *51*(10), 2639–2652.

Denyszyn, S. W., Fiorentini, M. L., Maas, R., & Dering, G. (2018). A bigger tent for CAMP. *Geology*, *46*(9), 823–826.

Downes, H. (1993). The nature of the lower continental crust of Europe: Petrological and geochemical evidence from xenoliths. *Physics of the Earth and Planetary Interiors*, *79*(1–2), 195–218.

Ducea, M. N., Kidder, S., Chesley, J. T., & Saleeby, J. B. (2009). Tectonic underplating of trench sediments beneath magmatic arcs: The central California example. *International Geology Review*, *51*(1), 1–26.

England, P. C., & Thompson, A. B. (1984). Pressure—temperature—time paths of regional metamorphism I. Heat transfer during the evolution of regions of thickened continental crust. *Journal of Petrology*, *25*(4), 894–928.

Ewing, T. A., Hermann, J., & Rubatto, D. (2013). The robustness of the Zr-in-rutile and Ti-in-zircon thermometers during high-temperature metamorphism (Ivrea-Verbano Zone, northern Italy). *Contributions to Mineralogy and Petrology*, *165*(4), 757–779.

Ewing, T. A., Rubatto, D., Beltrando, M., & Hermann, J. (2015). Constraints on the thermal evolution of the Adriatic margin during Jurassic continental break-up: U–Pb dating of rutile from the Ivrea–Verbano zone, Italy. *Contributions to Mineralogy and Petrology*, *169*(4), 44.

Fountain, D. M. (1976). The Ivrea—Verbano and Strona-Ceneri zones, Northern Italy: A cross-section of the continental crust—New evidence from seismic velocities of rock samples. *Tectonophysics*, *33*(1–2), 145–165.

Frost, B. R., & Chacko, T. (1989). The granulite uncertainty principle: Limitations on thermobarometry in granulites. *The Journal of Geology*, *97*(4), 435–450.

Galli, A., Grassi, D., Sartori, G., Gianola, O., Burg, J.-P., & Schmidt, M. W. (2019). Jurassic carbonatite and alkaline magmatism in the Ivrea zone (European Alps) related to the breakup of Pangea. *Geology*, *47*(3), 199–202.

Garber, J. M., Hacker, B. R., Kylander-Clark, A. R. C., Stearns, M., & Seward, G. (2017). Controls on trace element uptake in metamorphic titanite: Implications for petrochronology. *Journal of Petrology*, *58*(6), 1031–1057.

Garber, J. M., Rioux, M., Kylander-Clark, A. R., Hacker, B. R., Vervoort, J. D., & Searle, M. P. (2020). Petrochronology of Wadi Tayin metamorphic sole metasediment, with implications for the thermal and tectonic evolution of the Samail Ophiolite (Oman/UAE). *Tectonics*, *39*(12), e2020TC006135.

Garuti, G. (1980). The Ivrea-Verbano mafic ultramafic complex of the Italian western Alps: Discussion of some petrologic problems and a summary.

Green, E., Holland, T., & Powell, R. (2007). An order-disorder model for omphacitic pyroxenes in the system jadeite-diopside-hedenbergite-acmite, with applications to eclogitic rocks. *American Mineralogist*, *92*(7), 1181–1189.
Grove, M., Jacobson, C. E., Barth, A. P., & Vucic, A. (2003). Temporal and spatial trends of late cretaceous-early tertiary underplating of Pelona and related schist beneath southern California and southwestern Arizona. *Tectonic evolution of northwestern Mexico and the southwestern USA*, *374*, 381.
Guergouz, C., Martin, L., Vanderhaeghe, O., Thébaud, N., & Fiorentini, M. (2018). Zircon and monazite petrochronologic record of prolonged amphibolite to granulite facies metamorphism in the Ivrea-Verbano and Strona-Ceneri Zones, NW Italy. *Lithos*, *308*, 1–18.
Hacker, B., Kylander-Clark, A., & Holder, R. (2019). REE partitioning between monazite and garnet: Implications for petrochronology. *Journal of Metamorphic Geology*, *37*(2), 227–237.
Hacker, B. R., Kelemen, P. B., & Behn, M. D. (2011). Differentiation of the continental crust by relamination. *Earth and Planetary Science Letters*, *307*(3–4), 501–516.
Hacker, B. R., Kelemen, P. B., & Behn, M. D. (2015). Continental lower crust. *Annual Review of Earth and Planetary Sciences*, *43*, 167–205.
Halliday, A. N., Dickin, A. P., Hunter, R. N., Davies, G. R., Dempster, T. J., Hamilton, P. J., & Upton, B. G. (1993). Formation and composition of the lower continental crust: Evidence from Scottish xenolith suites. *Journal of Geophysical Research: Solid Earth*, *98*(B1), 581–607.
Hand, M., Scrimgeour, I., Powell, R., Stüwe, K., & Wilson, C. (1994). Metapelitic granulites from Jetty Peninsula, east Antarctica: Formation during a single event or by polymetamorphism? *Journal of Metamorphic Geology*, *12*(4), 557–573.
Handy, M., Franz, L., Heller, F., Janott, B., & Zurbriggen, R. (1999). Multistage accretion and exhumation of the continental crust (Ivrea crustal section, Italy and Switzerland). *Tectonics*, *18*(6), 1154–1177.
Handy, M. R. (1987). The structure, age and kinematics of the Pogallo fault zone; southern Alps, northwestern Italy. *Eclogae Geologicae Helvetiae*, *80*(3), 593–632.
Harlov, D. E., Wirth, R., & Hetherington, C. J. (2011). Fluid-mediated partial alteration in monazite: The role of coupled dissolution–reprecipitation in element redistribution and mass transfer. *Contributions to Mineralogy and Petrology*, *162*(2), 329–348.
Hart, R. J., Andreoli, M. A., Tredoux, M., & De Wit, M. J. (1990). Geochemistry across an exposed section of Archaean crust at Vredefort, South Africa: With implications for mid-crustal discontinuities. *Chemical Geology*, *82*, 21–50.
Heaman, L., Böhm, C. O., Machado, N., Krogh, T., Weber, W., & Corkery, M. (2011). The Pikwitonei granulite domain, Manitoba: A giant Neoarchean high-grade terrane in the northwest Superior province. *Canadian Journal of Earth Sciences*, *48*(2), 205–245.
Henk, A., Franz, L., Teufel, S., & Oncken, O. (1997). Magmatic underplating, extension, and crustal reequilibration: Insights from a cross-section through the Ivrea Zone and Strona-Ceneri Zone, northern Italy. *The Journal of Geology*, *105*(3), 367–378.
Hermann, J., Müntener, O., Trommsdorff, V., Hansmann, W., & Piccardo, G. B. (1997). Fossil crust-to-mantle transition, Val Malenco (Italian Alps). *Journal of Geophysical Research: Solid Earth*, *102*(B9), 20123–20132.
Hermann, J., & Rubatto, D. (2003). Relating zircon and monazite domains to garnet growth zones: Age and duration of granulite facies metamorphism in the Val Malenco lower crust. *Journal of Metamorphic Geology*, *21*(9), 833–852.
Holland, T., Baker, J., & Powell, R. (1998). Mixing properties and activity-composition relationships of chlorites in the system MgO-FeO-Al2O3-SiO2-H2O. *European Journal of Mineralogy*, 395–406.
Holland, T., & Powell, R. (1998). An internally consistent thermodynamic data set for phases of petrological interest. *Journal of Metamorphic Geology*, *16*(3), 309–343.
Holland, T., & Powell, R. (2003). Activity–composition relations for phases in petrological calculations: An asymmetric multicomponent formulation. *Contributions to Mineralogy and Petrology*, *145*(4), 492–501.
Hopper, J. R., & Buck, W. R. (1996). The effect of lower crustal flow on continental extension and passive margin formation. *Journal of Geophysical Research: Solid Earth*, *101*(B9), 20175–20194.
Horstwood, M. S., Foster, G. L., Parrish, R. R., Noble, S. R., & Nowell, G. M. (2003). Common-Pb corrected in situ U–Pb accessory mineral geochronology by LA-MC-ICP-MS. *Journal of Analytical Atomic Spectrometry*, *18*(8), 837–846.
Horstwood, M. S., Košler, J., Gehrels, G., Jackson, S. E., McLean, N. M., Paton, C., et al. (2016). Community-derived standards for LA-ICP-MS U-(Th-) Pb geochronology–Uncertainty propagation, age interpretation and data reporting. *Geostandards and Geoanalytical Research*, *40*(3), 311–332.
Jacobson, C. (1997). Metamorphic convergence of the upper and lower plates of the Vincent thrust, San Gabriel Mountains, southern California, USA. *Journal of Metamorphic Geology*, *15*(1), 155–165.
Jiao, S., Evans, N. J., Mitchell, R. N., Fitzsimons, I. C., & Guo, J. (2021). Heavy rare-earth element and Y partitioning between monazite and garnet in aluminous granulites. *Contributions to Mineralogy and Petrology*, *176*(7), 1–20.
Jochum, K. P., Stoll, B., Herwig, K., Willbold, M., Hofmann, A. W., Amini, M., et al. (2006). MPI-DING reference glasses for in situ microanalysis: New reference values for element concentrations and isotope ratios. *Geochemistry, Geophysics, Geosystems*, *7*(2), 44.
Karakas, O., Wotzlaw, J.-F., Guillong, M., Ulmer, P., Brack, P., Economos, R., et al. (2019). The pace of crustal-scale magma accretion and differentiation beneath silicic caldera volcanoes. *Geology*, *47*(8), 719–723.
Kay, R. W., & Mahlburg-Kay, S. (1991). Creation and destruction of lower continental crust. *Geologische Rundschau*, *80*(2), 259–278.
Kelsey, D., Clark, C., & Hand, M. (2008). Thermobarometric modelling of zircon and monazite growth in melt-bearing systems: Examples using model metapelitic and metapsammitic granulites. *Journal of Metamorphic Geology*, *26*(2), 199–212.
Klötzli, U. S., Sinigoi, S., Quick, J. E., Demarchi, G., Tassinari, C. C., Sato, K., & Günes, Z. (2014). Duration of igneous activity in the Sesia Magmatic System and implications for high-temperature metamorphism in the Ivrea–Verbano deep crust. *Lithos*, *206*, 19–33.
Kohn, M. J., & Vervoort, J. D. (2008). U-Th-Pb dating of monazite by single-collector ICP-MS: Pitfalls and potential. *Geochemistry, Geophysics, Geosystems*, *9*(4).
Kunz, B. E., Regis, D., & Engi, M. (2018). Zircon ages in granulite facies rocks: Decoupling from geochemistry above 850° C? *Contributions to Mineralogy and Petrology*, *173*(3), 26.
Kunz, B. E., & White, R. W. (2019). Phase equilibrium modelling of the amphibolite to granulite facies transition in metabasic rocks (Ivrea Zone, NW Italy). *Journal of Metamorphic Geology*, *37*(7), 935–950.
Lensch, G. (1972). Kelyphitperidotite in der mittleren Ivreazone zwischen Val d'Ossola und Val Strona. Ein Beitrag zur Herkunfstiefe der Ultramafitite der Ivreazone. *Schweiz Mineral. Petrogr Mitt*, *52*(2), 237–250.
Luvizotto, G., & Zack, T. (2009). Nb and Zr behavior in rutile during high-grade metamorphism and retrogression: An example from the Ivrea–Verbano zone. *Chemical Geology*, *261*(3–4), 303–317.
Mahar, E. M., Baker, J., Powell, R., Holland, T., & Howell, N. (1997). The effect of Mn on mineral stability in metapelites. *Journal of Metamorphic Geology*, *15*(2), 223–238.
Matzel, J. E., Bowring, S. A., & Miller, R. B. (2004). Protolith age of the Swakane Gneiss, North Cascades, Washington: Evidence of rapid underthrusting of sediments beneath an arc. *Tectonics*, *23*(6).

Mazzucchelli, M., & Siena, F. (1986). Geotectonic significance of the metabasites of the kinzigitic series, Ivrea-Verbano zone (Western Italian Alps). *Tschermaks Mineralogische und Petrographische Mitteilungen*, *35*(2), 99–116.
McKenzie, D., Nimmo, F., Jackson, J. A., Gans, P., & Miller, E. (2000). Characteristics and consequences of flow in the lower crust. *Journal of Geophysical Research: Solid Earth*, *105*(B5), 11029–11046.
Mehnert, K. (1975). The Ivrea Zone, a model of the deep crust. *Neues Jahrbuch für Mineralogie - Abhandlungen*, *125*, 156–199.
Ménard, G., & Molnar, P. (1988). Collapse of a Hercynian Tibetan plateau into a late Palaeozoic European basin and range province. *Nature*, *334*(6179), 235–237.
Morishita, T., Hattori, K. H., Terada, K., Matsumoto, T., Yamamoto, K., Takebe, M., et al. (2008). Geochemistry of apatite-rich layers in the Finero phlogopite–peridotite massif (Italian Western Alps) and ion microprobe dating of apatite. *Chemical Geology*, *251*(1–4), 99–111.
Mottram, C. M., Warren, C. J., Regis, D., Roberts, N. M., Harris, N. B., Argles, T. W., & Parrish, R. R. (2014). Developing an inverted Barrovian sequence; insights from monazite petrochronology. *Earth and Planetary Science Letters*, *403*, 418–431.
Palin, R., Searle, M., Waters, D., Parrish, R., Roberts, N., Horstwood, M., et al. (2013). A geochronological and petrological study of anatectic paragneiss and associated granite dykes from the D ay N ui C on V oi metamorphic core complex, N orth V ietnam: Constraints on the timing of metamorphism within the R ed R iver shear zone. *Journal of Metamorphic Geology*, *31*(4), 359–387.
Paquette, J. L., & Tiepolo, M. (2007). High resolution (5 μm) U–Th–Pb isotope dating of monazite with excimer laser ablation (ELA)-ICPMS. *Chemical Geology*, *240*(3–4), 222–237.
Paton, C., Hellstrom, J., Paul, B., Woodhead, J., & Hergt, J. (2011). Iolite: Freeware for the visualisation and processing of mass spectrometric data. *Journal of Analytical Atomic Spectrometry*, *26*(12), 2508–2518.
Pattison, D. R., Chacko, T., Farquhar, J., & McFarlane, C. R. (2003). Temperatures of granulite-facies metamorphism: Constraints from experimental phase equilibria and thermobarometry corrected for retrograde exchange. *Journal of Petrology*, *44*(5), 867–900.
Peressini, G., Quick, J., Sinigoi, S., Hofmann, A. W., & Fanning, M. (2007). Duration of a large mafic intrusion and heat transfer in the lower crust: A SHRIMP U–Pb zircon study in the Ivrea–Verbano zone (Western Alps, Italy). *Journal of Petrology*, *48*(6), 1185–1218.
Platt, J., & England, P. (1994). Convective removal of lithosphere beneath mountain belts-Thermal and mechanical consequences. *American Journal of Science*, *294*(3).
Putnis, A., & Putnis, C. V. (2007). The mechanism of reequilibration of solids in the presence of a fluid phase. *Journal of Solid State Chemistry*, *180*(5), 1783–1786.
Pyle, J. M., Spear, F. S., Rudnick, R. L., & McDonough, W. F. (2001). Monazite–xenotime–garnet equilibrium in metapelites and a new monazite–garnet thermometer. *Journal of Petrology*, *42*(11), 2083–2107.
Quick, J. E., Sinigoi, S., & Mayer, A. (1994). Emplacement dynamics of a large mafic intrusion in the lower crust, Ivrea-Verbano Zone, northern Italy. *Journal of Geophysical Research: Solid Earth*, *99*(B11), 21559–21573.
Quick, J. E., Sinigoi, S., & Mayer, A. (1995). Emplacement of mantle peridotite in the lower continental crust, Ivrea-Verbano zone, northwest Italy. *Geology*, *23*(8), 739–742.
Quick, J. E., Sinigoi, S., Snoke, A. W., Kalakay, T. J., Mayer, A., & Peressini, G. (2003). *Geologic map of the southern Ivrea-Verbano Zone, northwestern Italy*. US Geological Survey.
Rasmussen, B., & Muhling, J. R. (2007). Monazite begets monazite: Evidence for dissolution of detrital monazite and reprecipitation of syntectonic monazite during low-grade regional metamorphism. *Contributions to Mineralogy and Petrology*, *154*(6), 675–689.
Redler, C., Johnson, T., White, R., & Kunz, B. (2012). Phase equilibrium constraints on a deep crustal metamorphic field gradient: Metapelitic rocks from the Ivrea zone (NW Italy). *Journal of Metamorphic Geology*, *30*(3), 235–254.
Rivalenti, G. (1975). The origin of the Ivrea-Verbano basic formation (Western Italian Alps)-whole rock geochemistry. *Bollettino della Societa Geologica Italiana*, *94*, 1149–1186.
Rubatto, D., Chakraborty, S., & Dasgupta, S. (2013). Timescales of crustal melting in the Higher Himalayan Crystallines (Sikkim, Eastern Himalaya) inferred from trace element-constrained monazite and zircon chronology. *Contributions to Mineralogy and Petrology*, *165*(2), 349–372.
Rubatto, D., Hermann, J., & Buick, I. S. (2006). Temperature and bulk composition control on the growth of monazite and zircon during low-pressure anatexis (Mount Stafford, central Australia). *Journal of Petrology*, *47*(10), 1973–1996.
Rudnick, R., & Gao, S. (2014). *Composition of the continental crust in Treatise on Geochemistry editors-in-chief*, Heinrich Holland and Karl Turekian.
Rudnick, R., Gao, S., Holland, H., & Turekian, K. (2003). Composition of the continental crust. *The crust*, *3*, 1–64.
Rudnick, R. L., & Fountain, D. M. (1995). Nature and composition of the continental crust: A lower crustal perspective. *Reviews of Geophysics*, *33*(3), 267–309.
Sammon, L., Gao, C., & McDonough, W. (2020). Lower crustal composition in the southwestern United States. *Journal of Geophysical Research: Solid Earth*, *125*(3), e2019JB019011.
Sauer, K. B., Gordon, S. M., Miller, R. B., Vervoort, J. D., & Fisher, C. M. (2018). Provenance and metamorphism of the Swakane Gneiss: Implications for incorporation of sediment into the deep levels of the North Cascades continental magmatic arc, *Lithosphere*, *10*, 460–477.
Schaltegger, U., & Brack, P. (2007). Crustal-scale magmatic systems during intracontinental strike-slip tectonics: U, Pb and Hf isotopic constraints from permian magmatic rocks of the Southern Alps. *International Journal of Earth Sciences*, *96*(6), 1131–1151.
Schärer, U. (1984). The effect of initial 230Th disequilibrium on young UPb ages: The Makalu case, Himalaya. *Earth and Planetary Science Letters*, *67*(2), 191–204.
Schenk, V. (1990). The exposed crustal cross section of southern Calabria, Italy: Structure and evolution of a segment of Hercynian crust. In *Exposed cross-sections of the continental crust* (pp. 21–42). Springer.
Schmid, R., & Wood, B. (1976). Phase relationships in granulitic metapelites from the Ivrea-Verbano zone (Northern Italy). *Contributions to Mineralogy and Petrology*, *54*(4), 255–279.
Schmid, S. (1993). Ivrea zone and adjacent southern Alpine basement. In *Pre-mesozoic geology in the Alps* (pp. 567–583). Springer.
Schmid, S., Zingg, A., & Handy, M. (1987). The kinematics of movements along the Insubric line and the emplacement of the Ivrea zone. *Tectonophysics*, *135*(1–3), 47–66.
Schnetger, B. (1994). Partial melting during the evolution of the amphibolite-to granulite-facies gneisses of the Ivrea Zone, northern Italy. *Chemical Geology*, *113*(1–2), 71–101.
Siegesmund, S., Layer, P., Dunkl, I., Vollbrecht, A., Steenken, A., Wemmer, K., & Ahrendt, H. (2008). Exhumation and deformation history of the lower crustal section of the Valstrona di Omegna in the Ivrea Zone, southern Alps. *Geological Society, London, Special Publications*, *298*(1), 45–68.
Sills, J. D., & Tarney, J. (1984). Petrogenesis and tectonic significance of amphibolites interlayered with metasedimentary gneisses in the Ivrea Zone, Southern Alps, Northwest Italy. *Tectonophysics*, *107*(3–4), 187–206.

Sinigoi, S., Quick, J., Mayer, A., & Budahn, J. (1996). Influence of stretching and density contrasts on the chemical evolution of continental magmas: An example from the Ivrea-Verbano zone. *Contributions to Mineralogy and Petrology*, *123*(3), 238–250.
Smye, A. J., Lavier, L. L., Zack, T., & Stockli, D. F. (2019). Episodic heating of continental lower crust during extension: A thermal modeling investigation of the Ivrea-Verbano zone. *Earth and Planetary Science Letters*, *521*, 158–168.
Smye, A. J., & Stockli, D. F. (2014). Rutile U–Pb age depth profiling: A continuous record of lithospheric thermal evolution. *Earth and Planetary Science Letters*, *408*, 171–182.
Snoke, A. W., Kalakay, T. J., Quick, J. E., & Sinigoi, S. (1999). Development of a deep-crustal shear zone in response to syntectonic intrusion of mafic magma into the lower crust, Ivrea–Verbano zone, Italy. *Earth and Planetary Science Letters*, *166*(1–2), 31–45.
Stepanov, A. S., Hermann, J., Rubatto, D., & Rapp, R. P. (2012). Experimental study of monazite/melt partitioning with implications for the REE, Th and U geochemistry of crustal rocks. *Chemical Geology*, *300*, 200–220.
Taylor, S. R., & McLennan, S. M. (1985). *T*he continental crust: Its composition and evolution.
Tomascak, P. B., Krogstad, E. J., & Walker, R. J. (1996). U-Pb monazite geochronology of granitic rocks from Maine: Implications for late Paleozoic tectonics in the Northern Appalachians. *The Journal of Geology*, *104*(2), 185–195.
Truscott, M., & Shaw, D. (1990). Average composition of lower and intermediate continental crust, Kapuskasing Structural Zone, Ontario. In *Exposed cross-sections of the continental crust* (pp. 421–436). Springer.
Vavra, G., Gebauer, D., Schmid, R., & Compston, W. (1996). Multiple zircon growth and recrystallization during polyphase late Carboniferous to Triassic metamorphism in granulites of the Ivrea zone (Southern Alps): An ion microprobe (SHRIMP) study. *Contributions to Mineralogy and Petrology*, *122*(4), 337–358.
Vavra, G., & Schaltegger, U. (1999). Post-granulite facies monazite growth and rejuvenation during permian to lower Jurassic thermal and fluid events in the Ivrea zone (Southern Alps). *Contributions to Mineralogy and Petrology*, *134*(4), 405–414.
Vermeesch, P. (2018). IsoplotR: A free and open toolbox for geochronology. *Geoscience Frontiers*, *9*(5), 1479–1493.
Warren, C. J., Greenwood, L. V., Argles, T. W., Roberts, N. M., Parrish, R. R., & Harris, N. B. (2019). Garnet–monazite rare earth element relationships in sub-solidus metapelites: A case study from Bhutan. *Geological Society, London, Special Publications*, *478*(1), 145–166.
White, R., Powell, R., & Clarke, G. (2002). The interpretation of reaction textures in Fe-rich metapelitic granulites of the Musgrave block, central Australia: Constraints from mineral equilibria calculations in the system K2O–FeO–MgO–Al2O3–SiO2–H2O–TiO2–Fe2O3. *Journal of Metamorphic Geology*, *20*(1), 41–55.
White, R., Powell, R., & Holland, T. (2007). Progress relating to calculation of partial melting equilibria for metapelites. *Journal of Metamorphic Geology*, *25*(5), 511–527.
White, R., Powell, R., Holland, T., & Worley, B. (2000). The effect of TiO2 and Fe2O3 on metapelitic assemblages at greenschist and amphibolite facies conditions: Mineral equilibria calculations in the system K_2O-FeO-MgO-Al_2O_3-SiO_2-H_2O-TiO_2-Fe_2O_3. *Journal of Metamorphic Geology*, *18*(5), 497–511.
Whitney, D. L., & Evans, B. W. (2010). Abbreviations for names of rock-forming minerals. *American Mineralogist*, *95*(1), 185–187.
Yakymchuk, C., & Brown, M. (2014). Behaviour of zircon and monazite during crustal melting. *Journal of the Geological Society*, *171*(4), 465–479.
Yardley, B. W., & Barber, J. P. (1991). Melting reactions in the Connemara Schists: The role of water infiltration in the formation of amphibolite facies migmatites. *American Mineralogist*, *76*(5–6), 848–856.
Zanetti, A., Mazzucchelli, M., Sinigoi, S., Giovanardi, T., Peressini, G., & Fanning, M. (2013). SHRIMP U–Pb zircon Triassic intrusion age of the Finero mafic complex (Ivrea–Verbano Zone, Western Alps) and its geodynamic implications. *Journal of Petrology*, *54*(11), 2235–2265.
Zingg, A. (1980). Regional metamorphism in the Ivrea zone (Southern Alps, N Italy): Field and microscopic investigations.
Zingg, A., Handy, M., Hunziker, J., & Schmid, S. (1990). Tectonometamorphic history of the Ivrea zone and its relationship to the crustal evolution of the Southern Alps. *Tectonophysics*, *182*(1–2), 169–192.